December 2019

Theory of Extreme Optical Concentration in All-Dielectric Waveguides

Nazmus Sakib
Clemson University, nazmussakib102@yahoo.com

THEORY OF EXTREME OPTICAL CONCENTRATION IN ALL-DIELECTRIC WAVEGUIDES

A Thesis
Presented to
the Graduate School of
Clemson University

In Partial Fulfillment
of the Requirements for the Degree
Master of Science
Electrical Engineering

---

by
Nazmus Sakib
December 2019

Accepted by:
Dr. Judson D. Ryckman, Committee Chair
Dr. William R. Harrell
Dr. Hai Xiao

ABSTRACT

Dielectric waveguides are the solution to the ultra-fast optical communication. In all-dielectric waveguide systems, the boundary condition of Maxwell's electromagnetic equation can be exploited. Crucially dielectric materials have very low optical losses compared to metal hence the plasmonic structures. Due to very high losses, plasmonic structures are not suitable for practical usage. Achieving small mode dimensions has become an important factor in modern devices since smaller mode dimensions fosters high device density, efficiency, and or performance in a wide array of photonic systems. Keeping these criteria in focus, a transversely structured all-dielectric waveguide has been introduced in this thesis which exploits the vectorial nature of light to achieve extreme sub-wavelength confinement in high index dielectrics, enabling characteristic mode dimensions below $\lambda_0^2/1{,}000$ without metals or plasmonics. A new metric of performance measurement for waveguide structures has been introduced – "optical concentration". This metric of optical concentration has been derived and illustrated for its convenient usage in characterizing enhanced linear and nonlinear interactions at the nanoscale. This work expands the toolbox of nanophotonics and opens the door to new types of ultra-efficient and record performing linear and nonlinear devices with broad applications spanning classical and quantum optics.

ACKNOWLEDGMENTS

At first, I would like to show my gratitude and thank Dr. Judson D. Ryckman for giving me the opportunity to work on this novel project. He continuously supported me through his guidance, vision, theoretical and technical knowledge which helped me to overcome the difficulties and hindrance I faced working on this project. Without his supervision and advice this work would not be fruitful.

I would also like to acknowledge the help and support I received from my colleagues, Tahmid Hassan Talukdar, Farhan Bin Tarik and Cody Nelson towards my research work. From the simulation work to practical experiments, they have helped me in many stages of this project to make this a success and I hope I would get this support in future as well to continue on this project.

Finally, I would like to show my gratitude to the almighty for giving this opportunity to work, to keep me in health and grant me his blessing for continue working. I specially thank my committee members: Dr. William R. Harrell and Dr. Hai Xiao for their kind support and co-operation. I thank all the faculty members and staff of Holcombe Department of Electrical and Computer Engineering, Clemson University for supporting and co-operating me throughout my stay in Clemson.

This work was supported in part by a grant from the Air Force Office of Scientific Research (AFOSR) [program officer Dr. Gernot Pomrenke].

TABLE OF CONTENTS

Page

Table of Contents (Continued)

Page

LIST OF FIGURES

Figure Page

List of Figures (Continued)

Figure Page

CHAPTER 1

INTRODUCTION

1.1 Background

The waveguide is one of the most important and versatile building blocks utilized in electromagnetics and modern nanophotonics, where it is heavily relied on to enable advancements in opto-electronics [1], opto-mechanics [2], nonlinear optics [3–5], quantum photonics [6], nano-manipulation [7], and nano-sensing [8,9]. Waveguides capable of sub-wavelength light confinement are particularly advantageous for realizing ultra-efficient active photonic components such as classical and quantum light sources [10–14], phase/amplitude modulators [15–18], photodetectors [19], and atom-light interfaces [20].

Over the past two decades a large dichotomy between plasmonic and dielectric based photonics has emerged. To date, nanoplasmonic waveguides integrating metals are unrivalled in terms of achieving ultra-small mode dimensions [21–24]. However, ohmic losses result in significant passive propagation losses (~dB μm^{-1}) at optical frequencies which are untenable for many applications. Dielectric waveguides on the other hand, offer significantly lower passive propagation losses (~dB cm^{-1} to dB m^{-1}), yet are often implemented in resonant or slow-light structures in an effort to enhance temporal interaction and derive a larger response per unit energy. Dielectric resonators and band edge devices, however, are restricted to operating in narrow optical bandwidths and may require active resonant tuning to stabilize amidst

environmental variations – either of these factors may be prohibitive in certain applications.

1.2 Opto-electronic devices

Opto-electronic devices use both electrical and optical signals; and may convert electrical signals to optical signals or vice versa. These devices have opened new regimes of high speed and low-loss operation. One of the most important opto-electronic devices is the optical modulator which efficiently and rapidly encodes an electrical signal into an optical signal for data transmission. Optical integration is needed for the optical counterpart and electrical counterpart which is facilitated by the construction of on-chip optical modulators. Thus, optical modulators are one key component in silicon photonics [1].

Optical interconnects need to have high energy efficiency, low loss, low dispersion and low crosstalk. As technology advances, the number of optical interconnects in photonic devices increases. So, the complexity, density, and power consumption may increase. Copper interconnects have very high loss and dispersion. Optical modulators modulate the optical signal (electromagnetic beam) when travelling in free space or any optical waveguide. After modulation the beam properties (amplitude, phase and frequency) change. Modulation speed, optical bandwidth, insertion loss and power consumption are the important parameters need to be specified while using optical modulators [1].

Fig. 1.1 shows some opto-electronic device concepts. Fig. 1.1 (a) is the cross-section diagram of optical modulator based upon carrier accumulation [60]. Fig. 1.1 (b) is the carrier accumulation type device, this is a Mach-Zehnder interferometer

cross-section [60]. Fig. 1.1 (c) shows the cross-section of an electro-optic device for bandwidth greater than 50 GHz [61]. Fig. 1.1 (d) shows a plasmonic nano-rib waveguide [24].

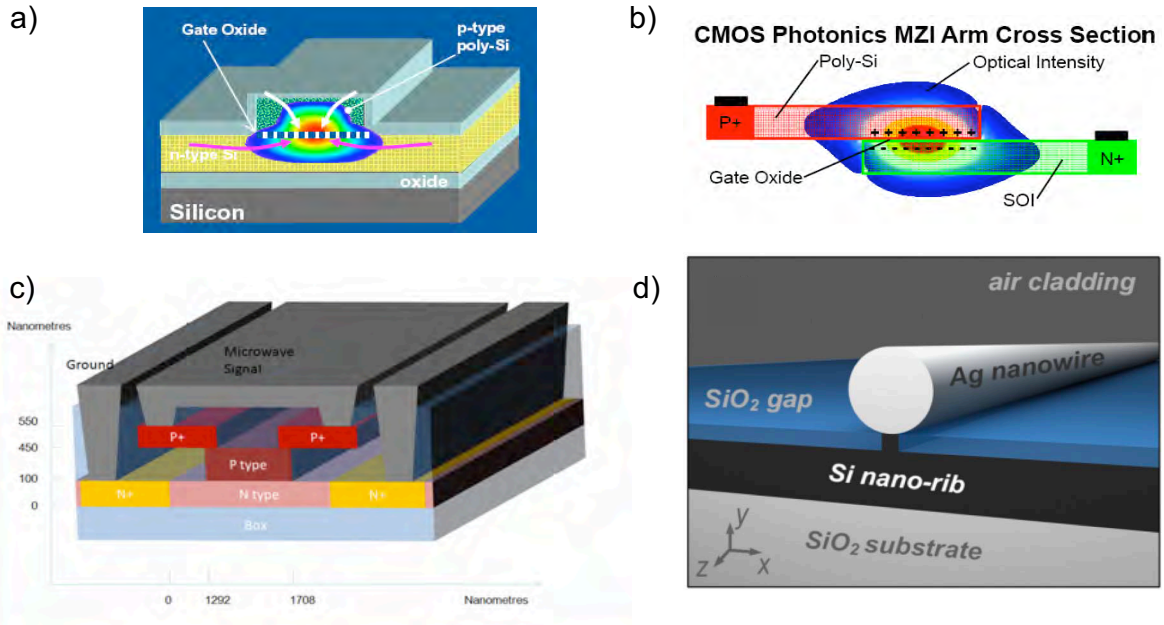

Fig. 1.1: Cross-section diagram of a) Optical modulator based upon carrier accumulation [60], b) Carrier accumulation type device [60]. c) Electro-optic device with bandwidth in excess of 50GHz [61], d) Hybrid nanowire-loaded silicon nano-rib plasmonic structure waveguide [24].

Below are some high-level key traits of optoelectronic modulators:

- Modulators used in optical interconnects ensure efficient and high bandwidth short and long range communication.
- Fabrication of optical interconnects and modulators are CMOS compatible.
- The use of transparent high refractive index semiconductors enables small, diffraction limited mode dimensions, high device efficiency and, compactness.

- There is a strong demand for ever more efficient devices capable of supporting higher data rate optical interconnection with lower power consumption.

1.3 Nonlinear optics

Photonic devices also offer the prospect of all-optical signal processing. To realize such functionality, nonlinear waveguides constructed from nonlinear optical materials are required. In the regime of nonlinear operation, the complex refractive index of a photonic device is modified by the presence of an optical signal. This influences optical transmission, thus enabling an all-optical signal processing operation. A wide variety of nonlinear physical phenomena become accessible when using compact waveguides with engineered properties. By using nonlinearities with ultra-fast response and recovery times, high bandwidth operations can be achieved.

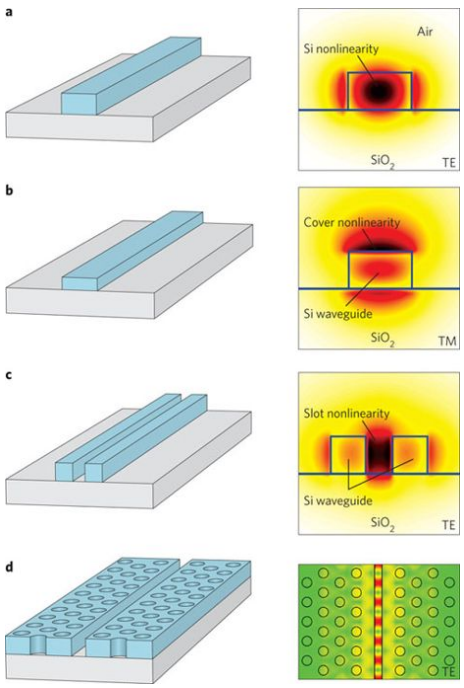

Fig. 1.2: Nonlinearity in photonic devices [4]

Photonic crystal structures offer this nonlinearity approach [3]. Fig. 1.2 shows the nonlinearity occurred in some photonic devices [4].

Quantum optics have demonstrated several methods of generating optical nonlinearities. These optical nonlinearities are achieved at the level of individual photons. Through strong photon-photon interactions, quantum-by-quantum control of light fields, single-photon switches and transistors, all optical deterministic quantum logic and strongly correlated states of light and matter can be realized [6].

In quantum optics, individual photons interact each other strongly such that light propagation depends on the number of photons. It is difficult to assume quantum operation in bulk optical material because of lower nonlinear coefficients. Quantum optics improve the performance of classical nonlinear devices. They enable fast energy-efficient optical transistors, without ohmic heating. Nonlinear switches using quantum optics can be used for optical quantum information processing and communication [6].

Fig. 1.3 shows the quantum nonlinearity in a cavity. Fig. 1.3 (a) shows the energy spectrum and Fig. 1.3 (b) shows the suppression of two photon transmission [6].

Below are some high level key traits of nonlinear optical waveguides:

- Nonlinear optics enables access to all-optical signal processing such as all-optical switching, frequency conversion and mixing, and comb generation.
- The performance of nonlinear devices is directly limited by the choice of active material, the local electric field intensity, and degree of light-matter interaction that is achieved.

- Performing nonlinear optics on-chip offers the advantages of compact and low-cost optical integration alongside nanoscale material and device engineering.
- There is a strong demand for ever more efficient nonlinear optical devices, requiring the realization of enhanced light-matter interactions in low loss and high-bandwidth platforms.

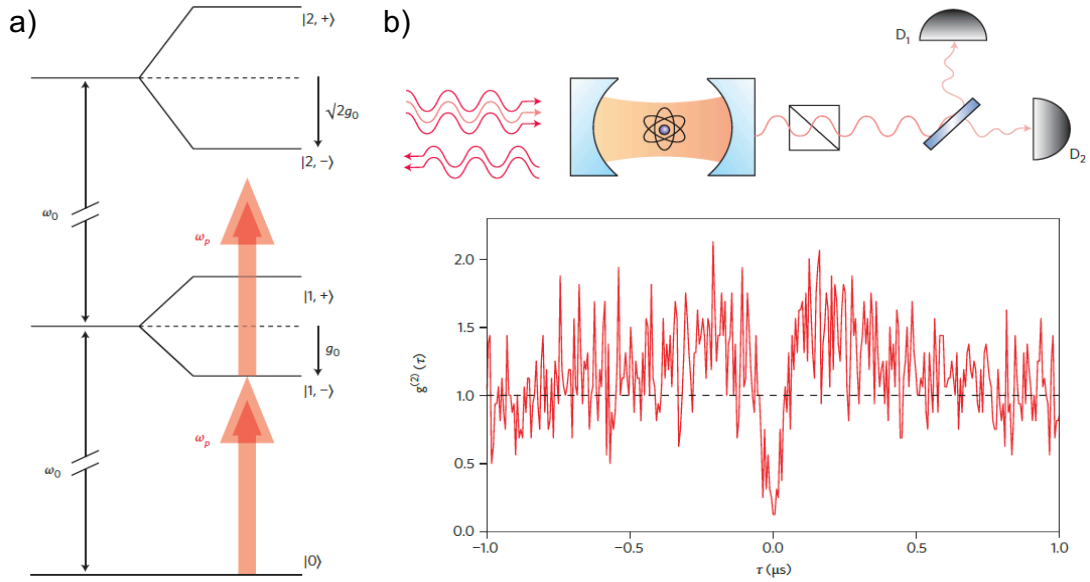

Fig. 1.3: Quantum nonlinear optics in a cavity, a) The energy spectrum, b) The suppression of two photon transmission [6]

1.4 Sensing

Optical sensing is another task which is directly facilitated by guided-wave optics. For example, nanosensing of surface-bound small molecules and other nanoscopic analytes can now be readily achieved using devices based on surface plasmon resonance, guided mode resonance, nanophotonic waveguide and resonators and 2D atomic materials. In sensing applications, when analytes or sensor

stimuli are introduced, local changes in complex refractive indices are introduced [8]. Hence, integrated optical waveguides attractively offer the opportunity for: (1) waveguide mode engineering to foster enhanced sensitivity, and (2) dense integration for compact and low-cost devices. Fig. 1.4 shows an example of optical sensor, this is a temperature sensor.

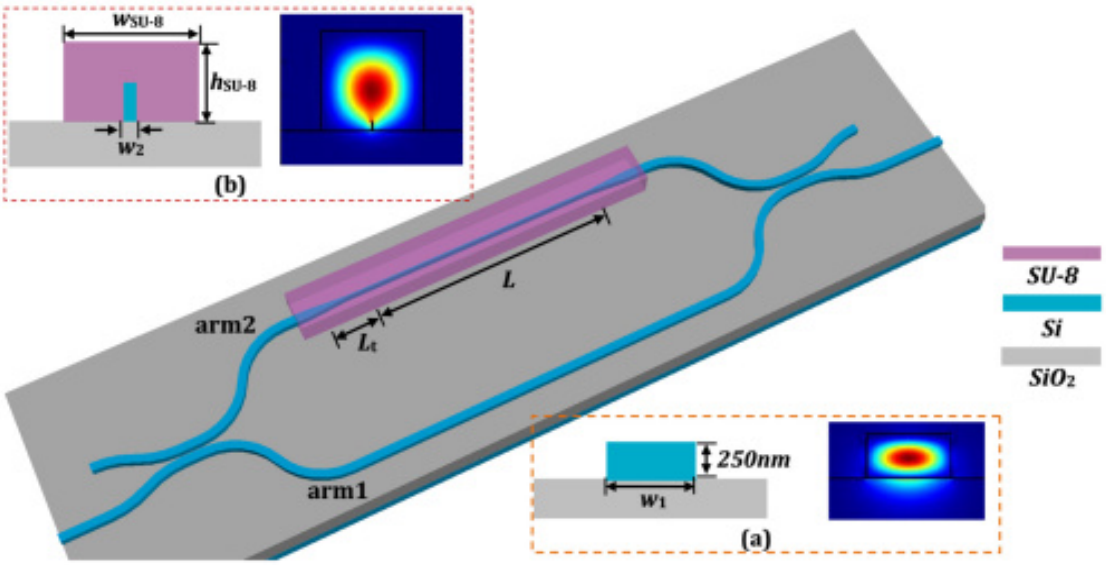

Fig. 1.4: Optical sensor with enhanced sensitivity [58]

1.5 Photodetectors

Photodetectors convert electromagnetic radiation to electric current, and are often realized from *p-n* junctions, which absorbs photons and generates electron-hole pairs in the depletion region. In standard CMOS fabrication process, germanium (Ge) is a prime material for making high performance telecom photodetectors. Ge has high absorption coefficient at 1.31 μm and at 1.5 μm wavelength. When the Ge

photodetector is evanescently coupled or butt-coupled to the Si waveguide, light is efficiently transferred to the Ge layer [19].

In a typical integrated photodetector design, a Ge absorber is overlaid on top of a Si waveguide. A thin dielectric layer may separate these two waveguide layers. The photodetector needs high bandwidth, low capacitance, high responsivity for optimal performance. By using thin Ge layer ensures higher bandwidth, but at the cost of lower mode confinement factor. This lower mode confinement factor leads to reduction in the responsivity of the photodetector. On the other hand, increasing the length will enable more light absorption but will also increase the capacitance and cause RC limitation to the bandwidth [19]. Hence, the optimization of waveguide integrated photodetectors requires maximizing light-matter interactions while simultaneously minimizing the size of the active absorbing region. Fig. 1.5 illustrates the schematics of Ge photodetector [19].

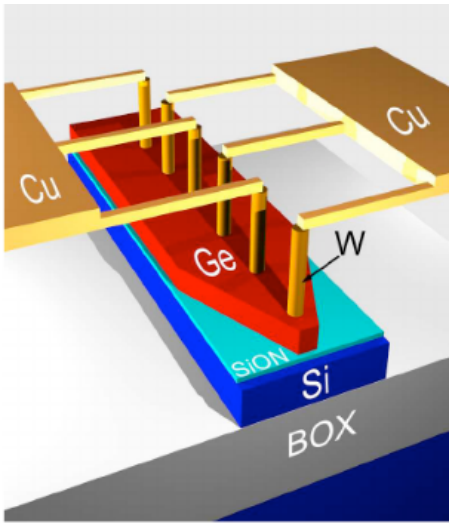

Fig. 1.5: Schematics of Ge photodetector consisting of Ge layer on top of Si film [19].

1.6 Evolution of guided optics

The evolution of guided optics starts from the introduction of optical fiber. Fig. 1.6 summarizes the evolution of guided optics in a topological order.

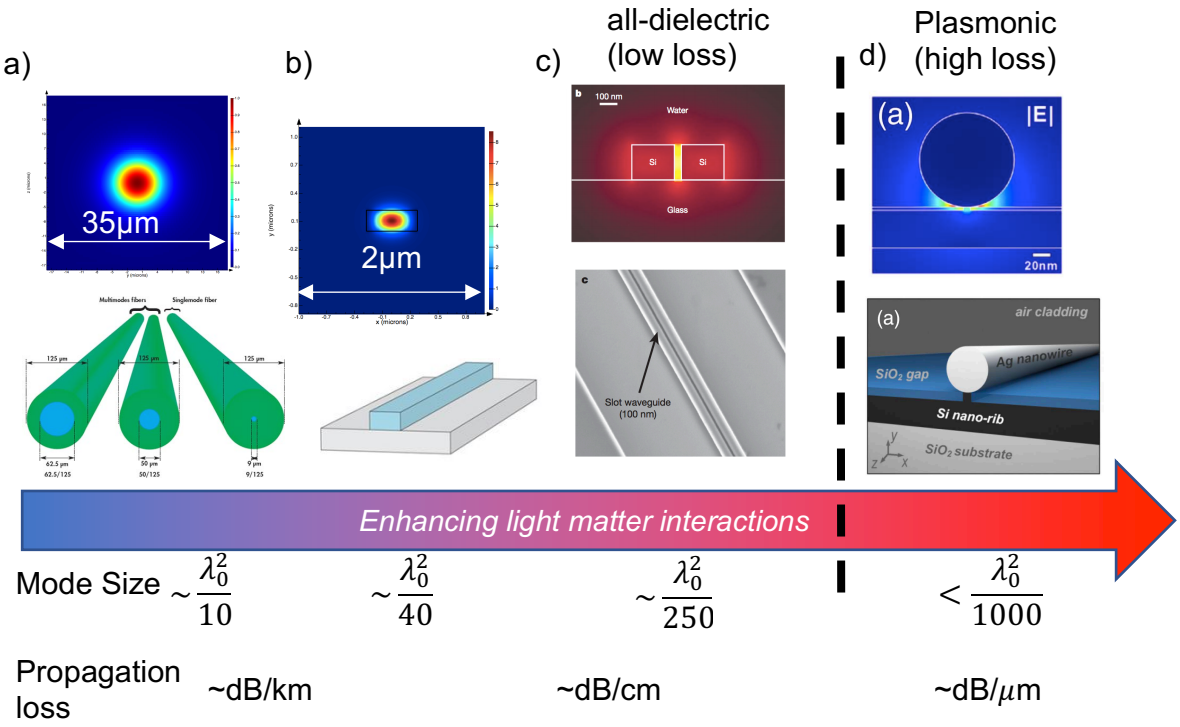

Fig. 1.6: Evolution of guided optics: a) Optical fiber [62], b) Strip waveguide [63], c) Slot waveguide [64], and d) Plasmonic waveguide [24]

Fig. 1.6 (a) shows the optical fiber, where the mode area is in the order of $(\sim\frac{{\lambda_0}^2}{10})$ and the propagation loss is in (~dB/km) [62]. The next phase is strip waveguide structure in Fig. 1.6 (b), where the mode area is in the order of $(\sim\frac{{\lambda_0}^2}{40})$, and the propagation loss is around (~dB/cm) [63] order which evolves into the all-dielectric slot waveguide structure in Fig. 1.6 (c), where the mode area is in the order of $(\sim\frac{{\lambda_0}^2}{250})$ [64].

Finally, the smallest mode area is obtained in the plasmonic structure in Fig. 1.6 (d) which is in the order of ($< \frac{{\lambda_0}^2}{1000}$), but the propagation loss becomes very high (in the range of ~dB/μm) [24]. This high propagation loss often renders the plasmonic waveguide structures unrealistic.

1.7 Organization Summary

The organization of this thesis is as follows:

- Chapter 2 discusses about the theoretical background using Maxwells's boundary equations and how they are being exploited in our proposed design structures. Also, the simulation results for the modal properties of these designs are presented.
- Chapter 3 gives an overview on "optical concentration". The definition and derivation of this metric is explored in this chapter. Linear interaction in the photonic devices and their relation to the optical concentration is discussed. The concept of "Purcell Factor" is elaborated in terms of optical concentration.
- Chapter 4 focuses on illuminating the connection between optical concentration and the characteristics of nonlinear devices. A detailed derivation is presented in this chapter.
- Chapter 5 presents the design and methods for numerical evaluation of various waveguide characteristics including optical concentration. Along with the methodology, the singularity at groove tip radius of curvature ($r = 0$) is summarized. The simulation results of optical concentration for the proposed diabolo and V-groove structures along with the optical concentration of the benchmarked plasmonic structure is presented and discussed.

- Finally, chapter 6 concludes this thesis with a conclusion and about the prospect of future research works leading to the reference section.

CHAPTER 2

DESIGN OF DIELECTRIC WAVEGUIDES WITH ULTRA-SMALL MODE DIMENSIONS

2.1 Design Preface

In this work, we theoretically explore an alternative waveguide architecture, capable of supporting enhanced nanoscale light concentration without the losses and bandwidth limitations of existing approaches. As recent all-dielectric metamaterial investigations to this same problem have recently indicated [25], we find that a promising yet largely unexplored regime exists in the case of high-index contrast media structured on the subwavelength scale. This regime specifically exploits the vectorial nature of light and enables the design of all-dielectric waveguides featuring extreme optical concentrations – a metric which is herein derived and related to both linear and nonlinear devices. Implications of such designs are considered and include record low optical mode areas and high Purcell factors for all-dielectric waveguides; ultra-low active volume (high index, e.g. solid-state) linear components; and, perhaps surprisingly, the simultaneously ability to either suppress or enhance core nonlinearity.

In order to achieve extreme optical concentration, a novel all-dielectric waveguide design has been developed. This design consists of a strip waveguide structure with “V” shaped groove inside it. The groove shape is associated with a 54.7-degree angle with the surface (the detail of the design will be discussed in the next sections). This V-groove structure is shown to yield very low optical mode areas with high Purcell factor. With these results, we have designed a more ambitious structure

with two “V” grooves resulting in a “diabolo” structure. From the simulation results, it has been found that this “diabolo” structure produces record low optical area with very high optical concentration (comparable with its Plasmonic counterpart) and high Purcell factor. Though this structure has very high optical concentration, these structures are theoretically lossless.

The design of these “V-groove” and “diabolo” structures consist of silicon core and silicon dioxide cladding region. The distance between the tip of the groove and bottom of the waveguide (in case of V-groove structure) and between the tips of two grooves (in case of “diabolo” structure) is defined as the height “h”. The design has been performed keeping in mind, that these structures are fabricable in clean room.

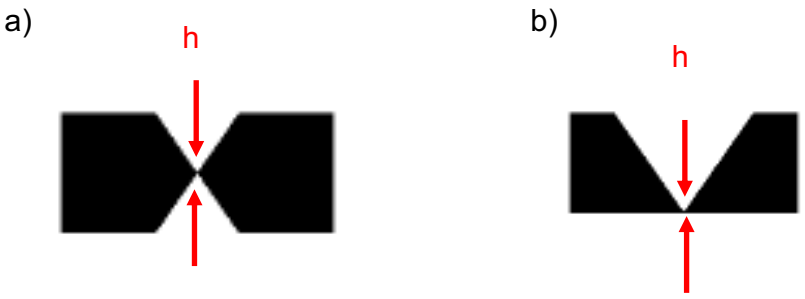

Fig. 2.1: Schematic design of a) Diabolo structure and b) V-groove structure

In this work, I have designed V-groove and diabolo structures in addition to conventional strip waveguide and slot waveguide in Lumerical to compare the characteristic parameters (optical mode area, nonlinear mode area, group index, effective index and confinement factor) by solving Maxwell’s boundary equations using Finite Differential Equation (FDE) method. The methods and results are discussed in

the following sections and chapters. The schematics of the V-groove and the diabolo structures are illustrated in Fig. 2.1.

2.2 Design Approach

In an inhomogeneous medium the mode solutions to Maxwell's equations are constrained by the presence of vectorial boundary conditions which must be enforced at all interfaces. Specifically, optical fields exhibit discontinuities in the normal component of electric field $\mathcal{E}$ and tangential component of displacement $\mathcal{D}$ at any interface with dielectric contrast ($\epsilon_h > \epsilon_l$) owing to the two boundary conditions, summarized here for non-dispersive dielectrics:

$$\mathcal{D}_{\perp,l} = \mathcal{D}_{\perp,h} \rightarrow \mathcal{E}_{\perp,l} = \frac{\epsilon_h}{\epsilon_l}\mathcal{E}_{\perp,h} \tag{2.1}$$

$$\mathcal{E}_{\parallel,h} = \mathcal{E}_{\parallel,l} \rightarrow \mathcal{D}_{\parallel,h} = \frac{\epsilon_h}{\epsilon_l}\mathcal{D}_{\parallel,l} \tag{2.2}$$

Fig. 2.2 illustrates simple configurations where these boundary conditions can enhance sub-wavelength optical concentration by locally enhancing the electric field energy density $u_E = \frac{1}{2}\boldsymbol{D} \cdot \boldsymbol{E}$. The first boundary condition, Eq. (2.1), requires continuity of the normal component of electric displacement and famously yields enhancement of the electric field in the low index medium, which is widely exploited in plasmonic and slot waveguides, e.g. Fig. 2.2(ii), under the appropriate field polarization [26–28]. While this 'slot effect' has proven to be especially useful for sensors [9], nanomanipulation in aqueous media [7], and low index integrated linear and nonlinear devices [18], it is not a particularly useful configuration for developing solid-state

components based on high index materials such as lasers [29], quantum emitters [30], phase/amplitude modulators [1,31], or photodetectors [19].

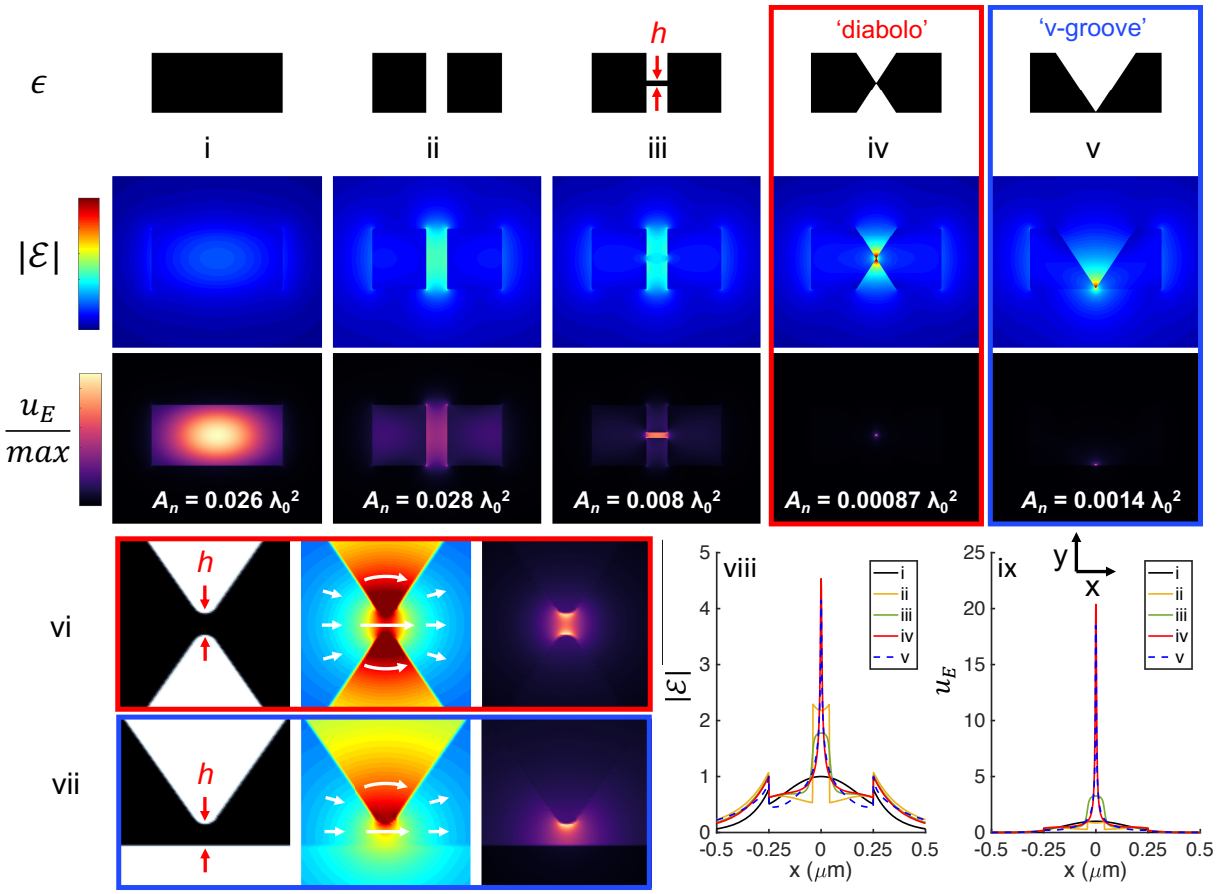

Fig. 2.2. Dielectric function, electric field (energy normalized, single color scale), and electric field energy density (peak normalized, individual color scales) for Si/SiO_2 waveguide quasi-TE fundamental modes simulated at $\lambda_0 = 1.55\ \mu m$: (i) strip (500 nm x 220 nm), (ii) slot (80 nm), (iii) bridged slot (80 nm, *h* = 20 nm), (iv) diabolo (*h* = 5 nm), and (v) V-groove (*h* = 5 nm) waveguides. (vi) and (vii) reveal a zoomed 40 nm x 40 nm view of (iv) and (v), including illustration of the local field vectors. (viii) Cross section of electric field and (ix) energy density (energy normalized where peak value of A is set to unity).

However, the second boundary condition Eq. (2.2), which has recently been highlighted and exploited in the design of ultra-low mode volume photonic crystal cavities [5,32,33], reveals that the electric displacement, and thus u_E, can be locally enhanced within a *high index* medium. If a narrow (h = 20 nm) high index bridge is introduced to span the slot (w = 80 nm) of a conventional slot waveguide, as shown in Fig. 2.2(iii), the predominant and already 'slot enhanced' $\mathcal{E}_x$ field component of the strongly polarized quasi-TE mode is carried through the high index bridge owing to continuity of the tangential component of the electric field. Such a configuration has a compound effect on the electric field energy density and effectively squares the energy density enhancement provided by the slot effect while enabling the peak optical energy density to carry into the high index medium. As a result, the local electric field energy density can be enhanced up to a total factor of approximately $(\epsilon_h/\,\epsilon_l)^2 = (n_h/n_l)^4$ relative to a homogenous waveguide core. This corresponds to a potential energy density enhancement (and mode area suppression) factor of ~30 for an oxide cladded silicon structure or ~150 for an air cladded device.

Designs which improve upon the bridged slot geometry of Fig. 2.2(iii) and better approach the ~$(n_h/\,n_l)^4$ enhancement factor limit may be achieved by tailoring the structure to enforce boundary Eq. (2.2) only where the slot effect is maximized, i.e. by using a diabolo or V-groove geometry as shown in Figs. 2.2(iv) and 2.2(v). These diabolo and V-groove designs function similar to plasmonic bow-ties and V-grooves [23], except they uniquely foster strong optical concentration in high index materials while providing the inherent advantages of low-loss all-dielectric media. For prototypical silicon/air and silicon/SiO_2 dielectrics considered here, we observe record

low waveguide mode areas, $A_n \sim \lambda_0^2/1{,}000$ to $\sim\lambda_0^2/10{,}000$, and high energy densities. The enhanced characteristics are observed to be a particularly strong function of the index contrast and high index 'bridge' height *h* (Fig. 2.3); and a weak function of the groove tip's nanoscaled radius of curvature *r* (Fig. 2.4).

2.3 Modal Characteristics and Analysis

Fig. 2.3 reports the modal characteristics of air and oxide cladded silicon diabolo and V-groove waveguides (e.g. from Fig. 2.2) as a function of the silicon bridge height *h*. In this analysis, the V-groove bottom cladding is fixed to oxide whereas a symmetrically distributed cladding material is considered for the diabolo geometry. As shown in Fig. 2.3 (a), the mode area A_n of both waveguides decreases significantly with decreasing *h*, reaching values in the range $A_n \sim \lambda_0^2/\ 1{,}000$ to $\sim\lambda_0^2/10{,}000$, more than one to two orders of magnitude below the diffraction limit for bulk silicon. The diabolo geometry is observed to enable the smallest values of A_n, which is attributed to the centered placement of the bridge and corresponding mode symmetry. Unlike slot waveguides which achieve $\sim(n_h/n_l)^2$ enhanced optical concentration solely in a low index medium, the V-groove and diabolo waveguides offer $\sim(n_h/n_l)^4$ enhancement in optical concentration (and $1/A_n$, F_P) in a *high index* medium. Also unlike a slot waveguide, the nanoscale bridge dimensions of these structures are expected to be compatible with the critical dimensions of standard photolithography (i.e. >150-300 nm) since the grooves can be realized by anisotropic wet etching of crystalline silicon [43,44].

Fig. 2.3(b) reports the nonlinear (NL) effective mode area $A_{eff}^{(NL)}$ for both waveguides, which is observed to exhibit substantially different characteristics and

trends with respect to refractive index contrast and waveguide geometry than the 'classic' mode area. In both structures evaluated in oxide claddings, reduction of *h* results in increasing values of $A_{eff}^{(NL)}$, indicative of nonlinearity *suppression*. Meanwhile in the air clad diabolo waveguide, record low values of $A_{eff}^{(NL)}$, smaller than any existing silicon nanowire geometry [45], not employing slow-light effects [46], are predicted.

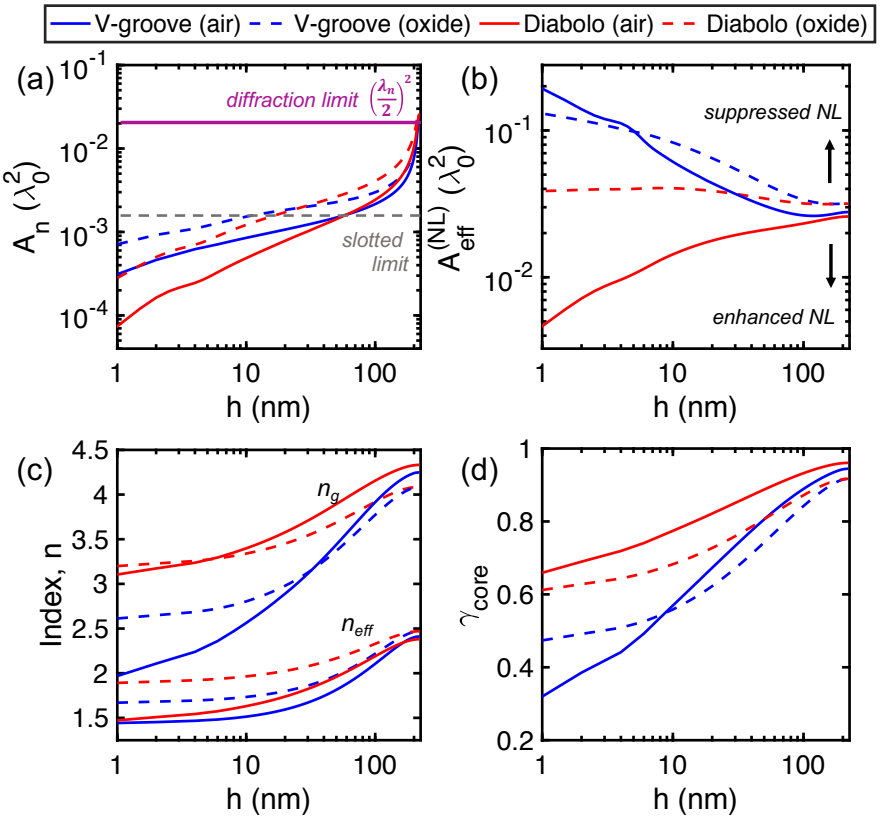

Fig. 2.3. All dielectric V-groove and diabolo waveguide modal characteristics as a function of bridge height *h*: (a) 'classic' mode area, (b) nonlinear effective mode area, (c) group and effective indices, and (d) core medium confinement factor. Note: *h* = 220 nm corresponds to an unmodified strip waveguide.

Here, the nonlinear mode area calculation assumes the nonlinearity arises strictly from the core material (e.g. silicon) in the approximation of single-mode degenerate four-wave mixing (FWM). Unlike linear 'matter-light' interaction metrics, which we've shown to be proportional or inversely proportional to optical concentration $U_{\mathcal{A}}$, the nonlinear mode area $A_{eff}^{(NL)}$ captures a distinctly different phenomenon of 'light-matter-light' interaction. An accurate description of $A_{eff}^{(NL)}$ in high-index inhomogenous media, is known to require a fully vectorial approach which accounts for the exact near-field distribution and group velocity [47,48]. In the literature however, there is generally no clear linkage between $A_{eff}^{(NL)}$ and other metrics used to characterize linear 'matter-light' interactions. We've recently derived such a linkage (see Chapter 4) and present an alternative formula for $A_{eff}^{(NL)}$, which is both rigorous and intuitive, and agrees with other fully vectorial reports [47,48]:

$$A_{eff}^{(NL)} = \frac{1}{(U_{\mathcal{A}}\mathcal{A})^2} \frac{\left(\iint_{\mathcal{A}} |\boldsymbol{\mathcal{E}}|^2 dA\right)^2}{\iint_{\mathcal{A}} |\boldsymbol{\mathcal{E}}|^4 dA} \tag{2.3}$$

where the term $U_{\mathcal{A}}\mathcal{A} = \Gamma_{\mathcal{A}}$. Unlike linear metrics (e.g. $A_n, F_P, \Gamma_{\mathcal{A}}$), the nonlinear effective mode area $A_{eff}^{(NL)}$ depends on the square of optical concentration and active area $\mathcal{A}$, with an additional corrective term that factors in the $|E|^4$ profile rather than simply the u_E profile.

For the core nonlinearity considered in Fig. 2.3(b), the active area $\mathcal{A}$ consists of the entire high index portion of the waveguide, e.g. $'core' = \mathcal{A} \rightarrow \mathcal{A}_{max}$. While both

u_E and $|E|^4$ are significantly enhanced in the vicinity of the bridge for small *h,* this local enhancement coincides with an overall reduction in $U_{core}\mathcal{A}_{max} = \left(\frac{n_g}{n_{core}}\right)\gamma_{core}$ as observable from Figs. 2.3(c) and 2.3(d). In the V-groove geometry this results in *suppressed* nonlinearity regardless of the cladding refractive index. Notably, in these devices it is possible to achieve a ~30-50x enhancement in a linear metric for a given medium, while simultaneously achieving a ~3x suppression in nonlinearity from the same medium. This unique capability is unachievable in low-index contrast optics and offers an attractive design solution to scaling the efficiency of linear optical devices while suppressing nonlinear performance impairments [49].

A simple explanation to this unique effect could be described as follows. In a linear device harnessing matter-light interaction, the active volume is defined by specifically engineering the geometry of the active material or region, which can be advantageously tailored on the nanoscale to be significantly smaller than the total dimensions of the waveguide core [34]. This enables high values of optical concentration $U_{\mathcal{A}}$ to be realized within the active area, assuming $\mathcal{A} < \mathcal{A}_{max}$. Nonlinearity on the other hand, implies that interactions are 'pumped' (light-matter effect) and 'probed' (matter-light effect) across the entire nonlinear medium. In the diabolo or V-groove waveguide geometries, *enhancement* in nonlinearity, relative to a strip waveguide, could be achieved only when: (1) the dominant nonlinear material is restricted to a small size, $\mathcal{A} < \mathcal{A}_{max}$, which is comparable to the region of enhanced u_E and $|E|^4$ (e.g. localized interactions with atoms, defects, nanomaterials); and/or (2)

the integrated $|E|^4$ enhancement term overcomes the Γ_{core}^2 suppression, as is apparent for the air-clad diabolo.

The high index contrast of the air clad diabolo waveguide results in a very large peak $|E|^4$ enhancement in silicon, which approaches with decreasing *h* a theoretical enhancement factor of $\sim(n_h/n_l)^8 \approx 2 \times 10^4$ relative to a homogenous silicon strip waveguide core. Thus, despite its lower transverse confinement factor γ_{core} and group index relative to a strip waveguide, the diabolo geometry enables significant reduction in $A_{eff}^{(NL)}$. For $h \approx 2$ nm, this corresponds to a record level fast-light nonlinear silicon waveguide parameter $\gamma \approx 1.5 \times 10^6$ W^{-1} km^{-1}. We also note the modal properties, including $A_{eff}^{(NL)}$ and thus the nonlinear parameter, are very weakly influenced by the V-groove tip's radius of curvature (Fig. 2.4). This nonlinearity enhancement is particularly impressive considering the width and height dimensions are unoptimized and that the non-linearity could be further enhanced in resonant [50] or slow-light configurations [46], if desired. In general however, waveguide systems exploiting highly localized non-linearities (atomic scale $\mathcal{A}$), such as those derived from silicon or germanium vacancy centers in diamond [51,52], would likely realize the most significant enhancements to nonlinearities.

In Fig. 2.4, the modal properties of air and SiO_2 cladded diabolo and v-groove waveguides as a function of groove tip radius of curvature *r* is also calculated. Here the silicon bridge height *h* is fixed to 2 nm. The results further validate our findings and show the modal properties are weakly affected by groove radius.

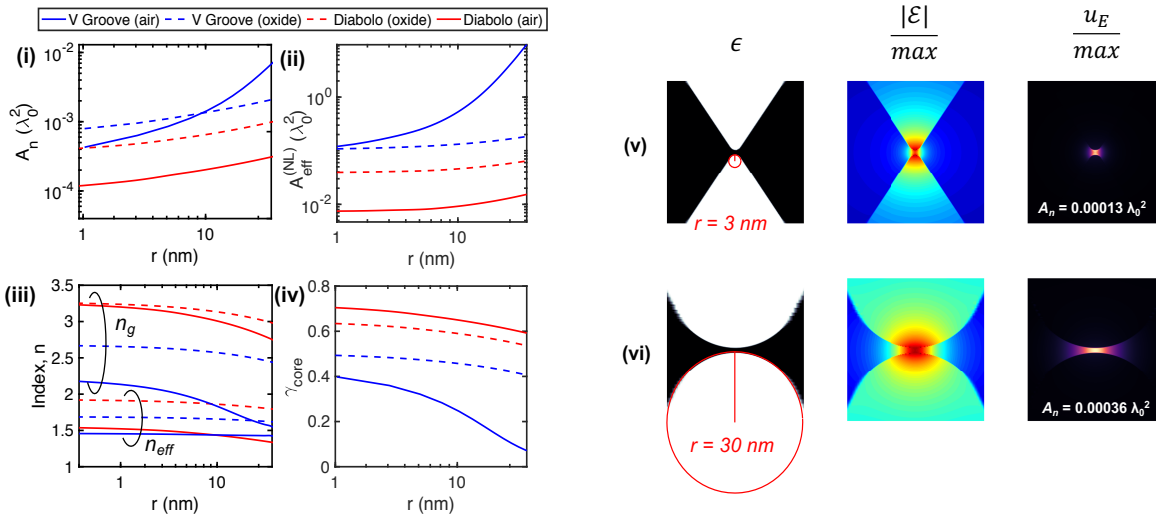

Fig. 2.4. Modal properties of V-groove and diabolo waveguides as a function of groove tip radius of curvature *r*. Here the silicon bridge height *h* is fixed to 2 nm.

CHAPTER 3

OPTICAL CONCENTRATION: A POWERFUL METRIC FOR USE IN NANOPHOTONICS

3.1 Overview of Optical Concentration

The concept of "optical concentration" is derived in the context of optical waveguides to assess the characteristics and implications of a waveguide with extreme electric field energy density enhancement. As discussed by Miller [34], optical concentration factor is a unifying yet underutilized metric which fundamentally limits the performance scaling in any active photonic device. The introduction of this concept importantly offers a simple framework (and intuitive alternative to invoking 'local density of states'), which unifies the disparate and sometimes limited metrics of: *i*) 'classic' mode area A_n, *ii*) Purcell factor F_P, *iii*) confinement factor Γ, and iv) nonlinear effective mode area $A_{eff}^{(NL)}$. A_n and F_P enable to quantify the enhancement in the spontaneous emission rate for a dipole (atomic scale volume) in a resonant mode field [35,36], yet they do not easily map to the characterization of different sorts of modern active photonic devices with arbitrary active volume dimensions. Similarly, optimization of Γ does not result in global minimization of active volume, but rather is strictly limited to minimization of device length *l*.

Optical concentration is related to the electromagnetic energy density that exists within an active material. A simple approach to illustrating optical concentration factor, is to measure the enhancement of electromagnetic energy density relative to some reference structure. In this way an optical concentration factor γ can be defined

as the ratio between the energy density confined in a structure to that of the reference, $\gamma = U_s/U_1$. This concept is illustrated in Fig. 3.1(a) [34]. Assuming a material of refractive index *n*, the wavelength inside this material is $\lambda_n = {}^{\lambda}/_{n}$ where λ is the free-space wavelength. For illustration purposes, the reference structure can be taken to be a dielectric waveguide with cross-sectional area ${\lambda_n}^2$. This is comparable to the minimum practical size of a diffraction limited dielectric structure. For accurate determination of the concentration factor, both the structure under study and the reference must assume the same unit input power. Hence, the optical concentration factor of the reference structure is by definition $\gamma = 1$. Optical concentration can be increased by either reducing the group velocity or reducing the waveguide cross-sectional area. If the group velocity is reduced, then the operating energy will be reduced and hence there will be an increase in the corresponding energy density in the active region. So, the optical concentration will be enhanced. On the other hand, if the waveguide cross-sectional area is reduced, then energy density increases so optical concentration increases [34].

Fig. 3.1(b) illustrates the optical concentration factor in a waveguide with cross-sectional area A_c which is different from the cross-sectional area of reference dielectric waveguide ${\lambda_n}^2$, $(A_c < {\lambda_n}^2)$. In this waveguide structure, due to smaller cross-sectional area, light propagation will be slower so in turn the group velocity will be reduced by a factor η. Group velocity, $v_g = {}^{c}/_{\eta n}$. This reduced group velocity enhances the optical concentration factor, $\gamma = \eta \frac{{\lambda_n}^2}{A_c}$ [34].

Fig. 3.1(c) illustrates a high finesse optical resonator with reflectivity *R*. This optical resonator increases the optical concentration factor to, $\gamma \approx \frac{1}{1-R} \approx \frac{\Im}{\pi}$, where $\Im$ is finesse and *R* is the reflectivity [34].

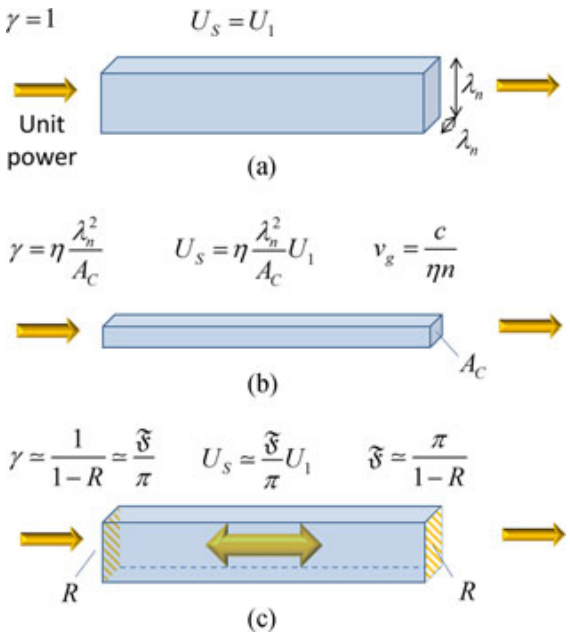

Fig. 3.1: Optical concentration factor γ, and electromagnetic energy density, U_s a) Reference device structure with size ${\lambda_n}^2$, $U_s = U_1$ b) waveguide with smaller cross-section, A_c with group velocity v_g c) A high-finesse resonator, $\mathfrak{F}$ finesse and R is reflectivity of mirror [34].

The illustration of Fig. 3.1 presents the concept of optical concentration and how it might be used in comparing optical components. However, a rigorous definition of "optical concentration" is, until now, still lacking from this literature. For example, the conceptual approach in Fig. 3.1 does not show how a rigorous calculation of the optical concentration in a reference structure may be made, nor does it precisely describe how to consider the effect of the electric field energy density vs. the magnetic

field energy density. In the following sections, we provide a first-principles derivation of optical concentration, which allows it to be computed directly and without measuring a 'factor' evaluated relative to a reference structure. This approach importantly also reveals how optical concentration is indeed closely linked to the physical operation and potential optimization of active photonic devices, and further allows us to demonstrate the direct connection between optical concentration and already existing metrics used to characterize light-matter interactions.

3.2 Derivation of Optical Concentration

The total electromagnetic energy density, u, may be defined as [37]:

$$u = \frac{1}{2}[\boldsymbol{D} \cdot \boldsymbol{E} + \boldsymbol{H} \cdot \boldsymbol{B}] \tag{3.1}$$

where the first term $\frac{1}{2}\boldsymbol{D} \cdot \boldsymbol{E}$ describes the electric field energy density u_E stored in a medium, including that in the propagating electric field and electric polarization, expressed here for local isotropic dielectric media as:

$$u_E = \frac{1}{2}\frac{\partial(\omega\varepsilon(\boldsymbol{r},\omega))}{\partial\omega}|\boldsymbol{E}(\boldsymbol{r},\omega,t)|^2 \approx \frac{1}{2}\varepsilon(\boldsymbol{r})|\boldsymbol{E}(\boldsymbol{r},t)|^2 \tag{3.2}$$

which simplifies to the right most expression in the approximation of minimally dispersive dielectric materials where $\varepsilon(\boldsymbol{r}) = \varepsilon_0\varepsilon_r(\boldsymbol{r})$ is the permittivity profile of the structure. (ε_0 is the permittivity of free space)

To quantify the important nature of the electric field energy density u_E in waveguides, and thus the resulting optical concentration, we reformulate the classic variational method applied to non-leaky waveguides [38], in terms of the electromagnetic energy density and a time average perturbation $\langle \Delta\tilde{u} \rangle$:

$$\Delta\tilde{\beta} = \frac{\omega \int \langle \Delta\tilde{u} \rangle dA}{\omega \int \langle (\partial u / \partial |\boldsymbol{k}|) \cdot \hat{z} \rangle dA} \tag{3.3}$$

This expression could be interpreted to quantify a complex change in power per unit length, normalized by the time averaged total energy flux across a plane perpendicular to the z-axis (unit power) [39], and should describe the complex phase shift of the wave in the z-direction per unit length. It has been shown that this type of variational approach leads directly to a rigorous derivation of the optical confinement factor $\Gamma_{\mathcal{A}}$ [40] (chapter 4) which satisfies:

$$\Delta\tilde{\beta} = \frac{\omega}{c} \Gamma_{\mathcal{A}} \Delta\tilde{n}_{\mathcal{A}} \tag{3.4}$$

where $\Delta\tilde{n}_{\mathcal{A}}$ is a complex index perturbation uniformly applied to an active area $\mathcal{A}$ in the waveguide cross-section.

Let us now consider an active waveguide device, with uniform cross-section and active area $\mathcal{A}$, which is extended along a propagation length l such that the total active volume is $\mathcal{V} = l\mathcal{A}$, as illustrated in Fig. 3.2. The total accumulated complex

phase response of a linear active device is proportional to the confinement factor times the device length:

$$\Delta\tilde{\beta} l \propto \Gamma_{\mathcal{A}} l \tag{3.5}$$

From this commonly utilized expression however, it is unclear how the device response scales or depends on the active volume $\mathcal{V}$. Given that the dimensions of active volume are a critical factor in real devices, for example in dictating the minimum energy consumption scaling of solid-state devices where energy can potentially be locally delivered to deeply sub-wavelength areas and volumes [34], it would be valuable to instead quantify the accumulated response $\Delta\tilde{\beta} l$ in terms of active volume $\mathcal{V}$.

Thus, we introduce a definition of optical concentration $U_{\mathcal{A}}$ [m^{-2}], consistent with Eq. (3.2) and (3.3) as:

$$U_{\mathcal{A}} \equiv \frac{\int_{\mathcal{A}} \langle u_E \rangle \, dA}{\mathcal{A}} \left(\frac{c}{n_{\mathcal{A}}}\right) \frac{2}{\omega \int \langle (\partial u / \partial |\boldsymbol{k}|) \cdot \hat{z} \rangle dA} \tag{3.6}$$

Which can alternatively be expressed (chapter 4) in relation to the rigorously defined confinement factor from:

$$U_{\mathcal{A}} = \frac{\Gamma_{\mathcal{A}}}{\mathcal{A}} = \eta \frac{1}{\mathcal{A}} \frac{\int_{\mathcal{A}} u_E dA}{\int u_E dA} = \eta \frac{\gamma_{\mathcal{A}}}{\mathcal{A}} \tag{3.7}$$

This newly defined metric of optical concentration captures both the effects of: i) longitudinal concentration via a factor $\eta = \frac{n_g}{n_{\mathcal{A}}}$, where n_g is the waveguide group index; and ii) transverse concentration via a factor $\frac{\gamma_{\mathcal{A}}}{\mathcal{A}}$, which computes the average electric field energy u_E in the active area per unit length, normalized to the total electric field energy per unit length [34]. Thus, it retains a clear dependence on u_E, which can be locally enhanced roughly two orders of magnitude in our diabolo and V-groove waveguide designs.

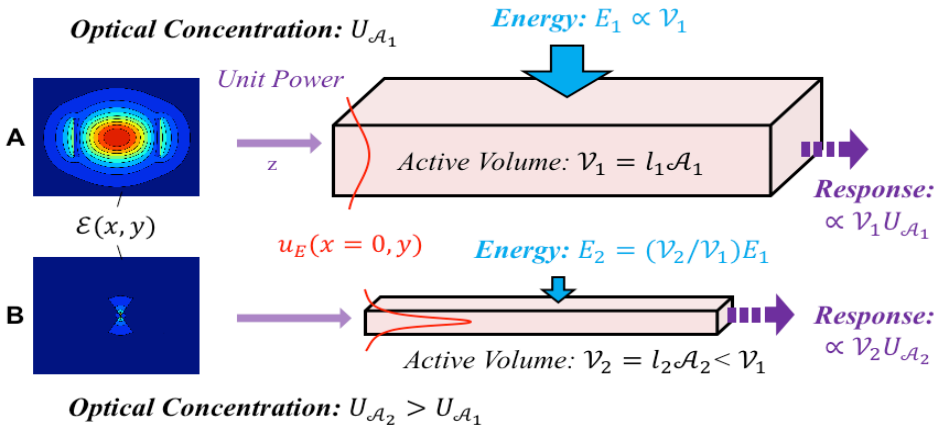

Fig. 3.2. Efficiency and active volume scaling principles. Under a constant desired linear-optic response, active volume is minimized when optical concentration $U_{\mathcal{A}}$ is maximized [34].

3.3 Optical response

With the optical concentration so-defined, the accumulated optical response originating from linear matter-light interaction now depends exactly on the product of the optical concentration and active volume:

$$\Delta\tilde{\beta} l = \frac{\omega}{c}\, U_{\mathcal{A}} \mathcal{V}\, \Delta\tilde{n}_{\mathcal{A}} \propto U_{\mathcal{A}} \mathcal{V} \tag{3.8}$$

The optical concentration is therefore the coefficient which satisfies the relations $\Delta n_{eff} l = \Delta n_{\mathcal{A}} U_{\mathcal{A}} \mathcal{V}$, $g_n l = g_{\mathcal{A}} U_{\mathcal{A}} \mathcal{V}$, and $\alpha_n l = \alpha_{\mathcal{A}} U_{\mathcal{A}} \mathcal{V}$, where Δn_{eff} is the perturbation in waveguide effective index arising from a perturbation $\Delta n_{\mathcal{A}}$ of the active region with active volume $\mathcal{V}$, and g_n or α_n are the modal gain or absorption coefficients imparted onto the waveguide mode from the gain or absorption coefficients $g_{\mathcal{A}}$ or $\alpha_{\mathcal{A}}$ of the active medium.

Unlike Eq. (3.4), the expression in Eq. (3.8) highlights a scaling principle which serves as a cornerstone of modern nanophotonics [34]. For a given material platform, reducing energy consumption in active devices requires simultaneous reduction in physical active volume $\mathcal{V}$ *and* enhancement of optical concentration $U_{\mathcal{A}}$, as illustrated in Fig. 3.2. Thus, the linear waveguide device operating with the smallest active volume does not necessarily feature the smallest device length and largest confinement factor, but rather exhibits the highest optical concentration $U_{\mathcal{A}}$.

With this framework in place, we can also consider more generally the problem of achieving a large waveguide optical concentration $U_{\mathcal{A}}$. A preferred solution would exhibit the following traits: (1) all-dielectric design to avoid the loss limitations associated with metals and plasmonics, (2) potential for broadband operation without relying on resonance or band edge effects, (3) achieves optical concentration in a high index material (e.g. semiconductor) to facilitate solid-state active components, and (4) potential compatibility with planar integrated photonics. While items (1-4) are fostered with our designs, as we will show, another elegant approach to this problem is

resonance-free light recycling [41,42]. Using a mode division multiplexing strategy this solution achieves a waveguide optical concentration which is the linear sum of the modal concentrations $U_{\mathcal{A}} = \sum_{n=1}^{N} U_{\mathcal{A},n}$ for each of the *N* forward and backward propagating modes superimposed in the structure. Assuming this strategy could be applied to ~6 spatial modes on each of 2 polarizations (e.g. *N* = 12), the waveguide concentration factor can be increased by approximately an order of magnitude while retaining a roughly constant active volume $\mathcal{V}$. However, this approach increases the accumulated waveguide loss by a factor on the order of ~*N* and in general may be restricted to configurations where the active area $\mathcal{A}$ is comparable to the diffraction limit $\sim(\lambda_n/2)^2$. In the waveguide designs under consideration here, we are exploring an alternative regime which achieves extreme optical concentrations $U_{\mathcal{A}}$ for sub-diffraction active areas, $\mathcal{A} < (\lambda_n/2)^2$.

For a given waveguide mode, the optical concentration $U_{\mathcal{A}}$ from Eqs. (3.6) or (3.7) is a strong function of both the particular placement and geometry of the active area $\mathcal{A}$ and the mode's energy density distribution u_E. Most photonic devices will employ a finite non-zero active area $\mathcal{A}$. In general terms however, the maximum theoretical optical concentration occurs in the case of an infinitesimal active area $\mathcal{A} \rightarrow dA$ centered at the location of maximum energy density $\boldsymbol{r}_{max}$, such that:

$$U_{\mathcal{A}\rightarrow dA}\big|_{\boldsymbol{r}=\boldsymbol{r}_{max}} = \frac{\eta}{A_n} \tag{3.9}$$

which recovers the appropriate definition of the 'classic' mode area A_n in non-leaky waveguides, applicable toward the calculation of the waveguide Purcell factor and in determining the enhancement of spontaneous emission for an emitter placed at $\boldsymbol{r}_{max}$ [36], where the mode area becomes:

$$A_n = \frac{\int u_{E_n} dA}{u_{E_n}(\boldsymbol{r}_{max})} \tag{3.10}$$

The Purcell factor in a waveguide is thus related directly to the optical concentration according to:

$$F_P = \left(\frac{3}{2\pi}\right)\lambda_n^2 U_{\mathcal{A}} \rightarrow \frac{3}{2\pi}\left(\frac{\eta}{\tilde{A}_n}\right) \tag{3.11}$$

where $\lambda_n = \lambda_0/n_{\mathcal{A}}$ and $\tilde{A}_n = A_n(\lambda_n)^{-2}$ is the normalized mode area in units of λ_n^2. In a broadband waveguide the longitudinal concentration factor remains $\eta = \frac{n_g}{n_{\mathcal{A}}}$. However, if the waveguide is formed into a standing wave cavity mode with finite finesse $\mathfrak{F}$, the on-resonance Purcell factor can be calculated by replacing the longitudinal factor η from Eq. (3.11) with $\eta = \mathfrak{F}/\pi$ to recover the famous $F_P \propto Q/V$ form [34–36]. The mode area A_n in our diabolo or V-groove waveguide, should therefore be suppressed, and F_P correspondingly enhanced, relative to a homogenous core waveguide by a factor approaching the maximum energy density enhancement factor $\sim(n_h/n_l)^4$.

Energy profile in any active devices depend on the physical active volume $\mathcal{V}$ and optical concentration $U_{\mathcal{A}}$. Smallest active volume does not always ensure the smallest device length, but it ensures the highest optical concentration. Optical concentration is a strong function of device geometry and mode's energy density distribution.

3.4 Linear Interactions and Their Relationship to "Optical Concentration"

The response of linear active waveguide devices may be described by a complex perturbation in wavevector according to [40]:

$$\Delta\beta = \Gamma_{\mathcal{A}}\left(\frac{\omega}{\mathrm{c}}\Delta n_{\mathcal{A}} + \frac{i}{2}\alpha_{\mathcal{A}}\right) = \Gamma_{\mathcal{A}}\left(\frac{\omega}{\mathrm{c}}\Delta n_{\mathcal{A}} - \frac{i}{2}g_{\mathcal{A}}\right) \tag{3.12}$$

Which as noted in Eq. (3.7) may be relayed in terms of optical concentration $U_{\mathcal{A}}$ per the relation:

$$U_{\mathcal{A}} = \Gamma_{\mathcal{A}}/\mathcal{A} \tag{3.13}$$

The derivation of these metrics, $\Gamma_{\mathcal{A}}$ and $U_{\mathcal{A}}$, uses the relation described in Eq. (3.3). The denominator of Eq. (3.3) describes the time averaged total energy flux across a plane perpendicular to the z-axis, and can be alternatively re-expressed for a travelling wave according to the relation:

$$\omega\int\langle(\partial u/\partial|\boldsymbol{k}|)\cdot\hat{z}\rangle dA = \frac{\partial\omega}{\partial k}\int 2\langle u_E\rangle dA \tag{3.14}$$

Which is a statement that energy flows at the group velocity $\frac{\partial \omega}{\partial k} = c/n_g$ and accounts for the total energy per unit length $\int \langle u \rangle dA$ being equal to twice the total electric field energy per unit length $2\int \langle u_E \rangle dA$. For non-magnetic optical devices ($\mu_r = 1$), local energy density perturbations are manifested strictly through material permittivity such that $\langle \Delta u \rangle = \langle \Delta u_E \rangle$. Therefore, in the approximation of low material dispersion the numerator of Eq. (3.3) can be re-expressed:

$$\omega \int \langle \Delta u_E \rangle dA = 2\omega \int \frac{\Delta \tilde{n}_{\mathcal{A}}(\boldsymbol{r})}{n_{\mathcal{A}}(\boldsymbol{r})} \langle u_E \rangle dA \tag{3.15}$$

Where $\Delta \tilde{n}_{\mathcal{A}}$ is a complex perturbation in material refractive index and $n_{\mathcal{A}}$ is the unperturbed refractive index. For a spatially invariant $\Delta \tilde{n}_{\mathcal{A}}$, occurring only in an active region $\mathcal{A}$, the index fraction may be pulled outside the integral.

Then substituting Eqs. (3.14) and (3.15) into Eq. (3.3) yields a solution consistent with Ref. [40]:

$$\Delta \tilde{\beta} = \frac{\omega}{c} \frac{n_g}{n_{\mathcal{A}}} \frac{\int_{\mathcal{A}} u_E dA}{\int u_E dA} \Delta \tilde{n}_{\mathcal{A}} \tag{3.16}$$

Which is equivalent with or without time averaging and recovers a form of the rigorously derived confinement factor $\Gamma_{\mathcal{A}}$, which is the coefficient that is known to satisfy Eq. (3.4). The accumulated response over some length *l* is therefore:

$$\Delta\tilde{\beta}l = \frac{\omega}{c}\Gamma_{\mathcal{A}}\Delta\tilde{n}_{\mathcal{A}}l = \frac{\omega}{c}\Gamma_{\mathcal{A}}\Delta\tilde{n}_{\mathcal{A}}\frac{\mathcal{V}}{\mathcal{A}} \tag{3.17}$$

This leads to Eq. (3.8). Where the optical concentration is the coefficient defined in Eq. (3.6) which follows from Eqs. (3.3, 3.14 - 3.17), and can also be expressed according to Eq. (3.7). For the case of a linear waveguide with continuous translational symmetry, it is convenient to utilize $U_{\mathcal{A}}$, whereas for a periodic waveguide (i.e. subwavelength grating, metamaterial, or photonic crystal) an alternative definition may be used. A perturbation in complex wavevector arising from a *linear* interaction is therefore:

$$\Delta\tilde{\beta} = U_{\mathcal{A}}\mathcal{A}\left(\frac{\omega}{c}\Delta n_{\mathcal{A}} + \frac{i}{2}\alpha_{\mathcal{A}}\right) = U_{\mathcal{A}}\mathcal{A}\left(\frac{\omega}{c}\Delta n_{\mathcal{A}} - \frac{i}{2}g_{\mathcal{A}}\right) \tag{3.18}$$

The complex phase shift accumulated over some propagation length *l* is therefore:

$$\Delta\tilde{\beta}l = U_{\mathcal{A}}\mathcal{A}l\left(\frac{\omega}{c}\Delta n_{\mathcal{A}} + \frac{i}{2}\alpha_{\mathcal{A}}\right) = U_{\mathcal{A}}\mathcal{A}l\left(\frac{\omega}{c}\Delta n_{\mathcal{A}} - \frac{i}{2}g_{\mathcal{A}}\right) \tag{3.19}$$

$$\Delta\tilde{\beta}l = U_{\mathcal{A}}\mathcal{V}\left(\frac{\omega}{c}\Delta n_{\mathcal{A}} + \frac{i}{2}\alpha_{\mathcal{A}}\right) = U_{\mathcal{A}}\mathcal{V}\left(\frac{\omega}{c}\Delta n_{\mathcal{A}} - \frac{i}{2}g_{\mathcal{A}}\right) \tag{3.20}$$

The complex phase shift, which is a determinizing characteristic of the active device response, is therefore proportional to the optical concentration and active volume:

$$\beta l_z \propto \mathcal{V} U_{\mathcal{A}} \tag{3.21}$$

This relationship expresses a clear scaling principle applicable in general to all linear photonic waveguide-based devices. It may be simply summarized as follows: for a constant stimulus (i.e. perturbation in material properties) and constant complex phase shift, minimization of the active device volume (which is principally proportional to the minimum energy consumption) requires maximization of the optical concentration $U_{\mathcal{A}}$.

3.5 Purcell Factor and Mode Area and Their Relationship to "Optical Concentration"

Taking the spontaneous emission rate Γ_s to be proportional to optical concentration $U_{\mathcal{A}}$, a simple definition of the Purcell factor in a waveguide could be made using a ratio of optical concentrations as:

$$F_P = \frac{\Gamma_s}{\Gamma_0} = \frac{U_{\mathcal{A}}}{U_0} \tag{3.22}$$

Which should agree with the conventionally defined Purcell factor under the appropriate reference concentration U_0. If considering only a single dipole at the field maximum, this relationship becomes

$$F_P = \frac{U_{\mathcal{A}\to dA}|_{\boldsymbol{r}=\boldsymbol{r}_{max}}}{U_0} = \frac{1}{U_0}\left(\frac{\eta}{A_n}\right) \tag{3.23}$$

Where A_n is the waveguide mode area:

$$A_n = \frac{\int u_{E_n} dA}{u_{E_n}(\boldsymbol{r}_{max})} \tag{3.24}$$

Per the approach taken by Miller, e.g. Ref. [34], it has been shown that the reference concentration U_0 may be described as $U_0 = \left(\frac{3}{2\pi}\right)\lambda_n^2$, where $\lambda_n = \frac{\lambda_0}{n}$ is the wavelength in the material with refractive index *n*. Substituting into Eq. (3.24) then yields the waveguide Purcell factor:

$$F_P = \left(\frac{3}{2\pi}\right)\lambda_n^2 U_A = \frac{3}{2\pi}\left(\frac{\eta}{\tilde{A}_n}\right) \tag{3.25}$$

Where the mode area can be normalized into units of λ_n^2 according to

$$\tilde{A}_n = \frac{\int u_{E_n} dA}{u_{E_n}(\boldsymbol{r}_{max})}\left(\frac{n(\boldsymbol{r}_{max})}{\lambda}\right)^2 \tag{3.26}$$

If the waveguide is formed into a cavity, then the concentration enhancement provided by the η term is replaced with a factor $\mathfrak{F}/\pi$, where $\mathfrak{F}$ is the cavity finesse [34].

$$F_P = \frac{3}{2\pi^2}\left(\frac{\mathfrak{F}}{\tilde{A}_n}\right) \tag{3.27}$$

In high-finesse cavities the finesse and Q-factor are related according to:

$$\mathfrak{F} = \frac{\lambda_n Q}{2L} \tag{3.28}$$

Therefore, the Purcell factor becomes:

$$F_P = \frac{3}{4\pi^2}\left(\frac{Q}{\tilde{A}_n}\right)\frac{\lambda_n}{L} = \frac{3}{4\pi^2}\left(\frac{Q}{\tilde{V}_n}\right) \tag{3.29}$$

Which recovers the classic unitless definition of the Purcell factor in terms of mode volume $\tilde{V}_n$ normalized into units of λ_n^3.

CHAPTER 4

OPTICAL CONCENTRATION IN THE CONTEXT OF NONLINEAR DEVICES

In the previous chapter, the concept of a new figure of merit "optical concentration" has been introduced and derived in the context of linear interactions in the active region of photonic devices. In this chapter, optical concentration will be explored in the context of nonlinear interaction in the active regions.

Nonlinear interaction is the base for important photonic devices (e.g. degenerate four-wave mixing, self-phase modulation, two photon absorption in bulk optical media). Thus, this new metric "Optical Concentration" needs to be defined for the nonlinear interaction. This will help analyze the behavior and characteristics of these nonlinear photonic devices.

4.1 Nonlinear Interactions and Their Relationship to "Optical Concentration"

Nonlinear interactions, can be described by an intensity [W/m^2] dependent complex perturbation in complex wave vector:

$$\Delta k = \left(\frac{\omega}{c}\Delta n_{NL} + \frac{i}{2}\alpha_{NL}\right) \tag{4.1}$$

Where the change in material index can be described by:

$$\Delta n_{NL} = n_2 I = n_2 \frac{P}{A} \tag{4.2}$$

Here the underlying physics of, for example, a $\chi^{(3)}$ process and intensity dependent polarization describing the light-matter interaction, are simply captured in a macroscopic model, where n_2 is a material property [RIU m^2 / W], and *I* is the optical intensity in the material [W / m^2], which could alternatively be described by the input optical power *P* [W] divided by an area *A* [m^2].

The nonlinearly induced absorption coefficient may similarly be described by:

$$\alpha_{NL} = \beta_T I = \beta_T \frac{P}{A} \tag{4.3}$$

Here the underlying physics (i.e. mediated by two-photon absorption) are again captured in a macroscopic model via a material coefficient β_T [m / W]. A nonlinear coefficient γ can thus be simply defined by factoring the input power P out of the complex perturbation in complex wavevector:

$$\tilde{\gamma} \equiv \frac{\Delta k}{P} = \left(\frac{\omega}{c}\Delta n_{NL} + \frac{i}{2}\alpha_{NL}\right)/P \tag{4.4}$$

$$\tilde{\gamma} = \frac{1}{A}\left(\frac{\omega}{c}n_2 + \frac{i}{2}\beta_T\right) \tag{4.5}$$

In an optical waveguide the nonlinear coefficient captures the complex perturbation $\Delta\tilde{\beta}$ in the waveguide's complex wavevector $\tilde{\beta}$.

$$\tilde{\gamma} = \frac{\Delta\tilde{\beta}}{P} = \left(\frac{\omega}{c}\Delta n_{eff,NL} + \frac{i}{2}\alpha_{eff,NL}\right)/P \tag{4.6}$$

By treating the coefficients n_2 and β_T as material parameters (which are valid under the general macroscopic form of Maxwell's equations) we can write the nonlinear coefficient in terms of a nonlinear effective mode area $A_{eff}^{(NL)}$ [m^2]:

$$\tilde{\gamma} = \frac{1}{A_{eff}^{(NL)}}\left(\frac{\omega}{c}n_2 + \frac{i}{2}\beta_T\right) \tag{4.7}$$

Clearly the nonlinear parameter is maximum when $A_{eff}^{(NL)}$ is minimized and vice versa. An exact and correct calculation of $A_{eff}^{(NL)}$ is therefore crucial to assist in designing optical devices to either enhance or suppress non-linear effects. One definition of nonlinear mode area is:

$$A_{eff}^{(i)} = \frac{\left(\iint_{\infty} |\boldsymbol{\mathcal{E}}_{\boldsymbol{n}}(\boldsymbol{r})|^2 dA\right)^2}{\iint_{NL} |\boldsymbol{\mathcal{E}}_{\boldsymbol{n}}(\boldsymbol{r})|^4 dA} \tag{4.8}$$

However, this expression is only valid in the limit of vanishing index contrast $(n_H - n_L) \approx 0$ and vanishing contrast between material and waveguide group indices $(n_{g,NL} - n_{g,wvg}) \approx 0$, a regime which is clearly inapplicable to most integrated optical devices. A correct expression for $A_{eff}^{(NL)}$ crucially requires accounting for the fully vectorial nature of wave propagation and the power and/or energy distribution

and confinement in the waveguide. Only very recently has a correct fully vectorial mode area been derived from Maxwell's equations and supported experimentally, [47]:

$$A_{eff}^{(f)} = \frac{3\left(\iint_{\infty} n(\boldsymbol{r})^2 |\boldsymbol{\mathcal{E}}|^2 dA\right)^2}{n_{g,wvg}^2 n_H^2 \iint_{NL:n=n_H} \boldsymbol{\mathcal{E}}^* \cdot [2|\boldsymbol{\mathcal{E}}|^2 \boldsymbol{\mathcal{E}} + (\boldsymbol{\mathcal{E}} \cdot \boldsymbol{\mathcal{E}})\boldsymbol{\mathcal{E}}^*] dA} \tag{4.9}$$

However, the calculation in this exact form is rather cumbersome and does not provide clear linkage to other common metrics such as confinement factor or our metric of optical concentration. Here we independently derive an alternative expression for $A_{eff}^{(NL)}$, which fully considers the aforementioned criteria, and present it in an easily calculable form accessible to most researchers. Further, we identify for the first time, a clear relationship between the exact vectorial nonlinear mode area and a rigorous definition of the optical confinement factor used in linear optics. This suggests the nonlinear parameter and mode area can be determined from experimental measurement of the *linear* confinement factor paired with a calculable *nonlinear* correction factor.

Our derivation of $A_{eff}^{(NL)}$ relies on the macroscopic form of Maxwell's equations describing the fully vectorial nature of electromagnetic propagation and confinement and takes the assumption of single-mode degenerate four wave mixing (FWM) such that a single field profile may be considered. Recall from the previous chapter regarding linear matter-light interactions, inducing a complex perturbation $\Delta\beta$ to the waveguide wavevector β according to Eq. (3.12). In this form $\Delta n_{\mathcal{A}}$ and $\alpha_{\mathcal{A}}$ are treated

as perturbations of the unperturbed material properties such that its refractive index is perturbed uniformly within the active region $\mathcal{A}$ according to $\tilde{n} = n + \Delta\tilde{n}$, where $\Delta\tilde{n} = \Delta n_{\mathcal{A}} + i\frac{4\pi}{\lambda}\alpha_{\mathcal{A}} = \Delta n_{\mathcal{A}} - i\frac{4\pi}{\lambda}g_{\mathcal{A}}$. The confinement factor $\Gamma_{\mathcal{A}}$ is therefore the coefficient which satisfies:

$$\Delta\tilde{\beta} = \frac{\omega}{c}\Delta\tilde{n}\Gamma_{\mathcal{A}} = \frac{\omega}{c}\Delta\tilde{n}_{eff} \tag{4.10}$$

$$\Delta\tilde{n}_{eff} = \Delta\tilde{n}\Gamma_{\mathcal{A}} \tag{4.11}$$

The confinement factor often appears in the literature incorrectly as a measure of fraction of total electromagnetic power propagating along the z-axis confined in the active region (using either integrated Poynting vector or field intensity) normalized to the total electromagnetic power propagating along the z-axis. Such expressions are only valid only in the limit of vanishing index contrast $(n_H - n_L) \approx 0$ and vanishing contrast between material and waveguide group indicies $(n_{g,NL} - n_{g,wvg}) \approx 0$. The correct form of the confinement factor, which has been derived via the variational principle, e.g. Eq. (3.16) and Ref. [40], and has been shown to capture the physics of fully vectorial fields and modal dispersion in high index contrast media can also be written as:

$$\Gamma_{\mathcal{A}} = \frac{n_{\mathcal{A}} c\epsilon_0 \iint_{\mathcal{A}} |\boldsymbol{\mathcal{E}}|^2 dA}{\iint_{\infty} Re\{\boldsymbol{\mathcal{E}} \times \boldsymbol{\mathcal{H}}^*\} \cdot \hat{\boldsymbol{z}} dA} \tag{4.12}$$

which is a measure of field intensity confined to the active region normalized to unit power. Although it may not appear obvious, this expression does in fact capture the effect of the waveguide group index n_g,

$$n_g = \frac{c \iint_\infty \frac{1}{2}\frac{\partial}{\partial \omega}(\omega\epsilon)|\boldsymbol{\mathcal{E}}|^2 dA}{\frac{1}{2}\iint_\infty Re\{\boldsymbol{\mathcal{E}} \times \boldsymbol{\mathcal{H}}^*\} \cdot \hat{\boldsymbol{z}} dA} \tag{4.13}$$

which can rigorously be calculated even from a single frequency mode calculation if the frequency dependence of the permittivity term is included in the calculation, or more readily if material dispersion is small such that $\frac{\partial}{\partial \omega}(\omega\epsilon) = \epsilon$. In such a case $\Gamma_{\mathcal{A}}$ can be written as:

$$\Gamma_{\mathcal{A}} = \frac{n_g \iint_{\mathcal{A}} u_E dA}{n_A \iint_\infty u_E dA} \tag{4.14}$$

Use of the confinement factor, however, assumes that the perturbation is strictly uniform through the active region. In a nonlinear interaction, the local index change is proportional to the local electric field intensity $|E|^2$. Thus $\Delta\tilde{n}_{\mathcal{A}}$ is not uniform or constant across the active region and instead should be kept inside the integral, unlike Eq. (3.6), such that we write:

$$\Delta\tilde{\beta} = \frac{\omega}{c}\frac{n_g}{n_{\mathcal{A}}}\frac{\int \Delta\tilde{n}_{\mathcal{A}}(x,y)u_E dA}{\int u_E dA} \tag{4.15}$$

Or equivalently:

$$\Delta\tilde{\beta} = \frac{\omega}{c}\frac{n_{\mathcal{A}} c\epsilon_0 \iint_{\mathcal{A}} \Delta\tilde{n}_{\mathcal{A}}(x,y)|\boldsymbol{\mathcal{E}}|^2 dA}{\iint_{\infty} Re\{\boldsymbol{\mathcal{E}} \times \boldsymbol{\mathcal{H}}^*\} \cdot \hat{\mathbf{z}} dA} \tag{4.16}$$

This expression assumes only that the unperturbed refractive index $n_{\mathcal{A}}$ is uniform within the active region. The complex index change within the waveguide cross-section can be written as:

$$\Delta\tilde{n}_{\mathcal{A}}(x,y) = \left(\mathrm{n}_2 + i\frac{4\pi}{\lambda_0}\beta_T\right) I(x,y) \tag{4.17}$$

where the local electric field intensity function $I(x,y)$ [W/m^2] can be expressed in terms of the input power *P* according to:

$$I(x,y) = \frac{n_{\mathcal{A}} c\epsilon_0 |\boldsymbol{\mathcal{E}}(x,y)|^2}{\iint_{\infty} Re\{\boldsymbol{\mathcal{E}} \times \boldsymbol{\mathcal{H}}^*\} \cdot \hat{\mathbf{z}} dA}\ P \tag{4.18}$$

The complex change in wave-vector therefore captures both the light-matter interaction which induces the complex change in material refractive indices and the matter-light interaction which translates the change in material indices into a complex change in propagation constant, and can be expressed as either:

$$\Delta\tilde{\beta} = \frac{\omega}{c}\left(\mathrm{n}_2 + i\frac{4\pi}{\lambda_0}\beta_T\right)\left[\frac{n_g}{n_{\mathcal{A}}}\frac{\int \frac{n_{\mathcal{A}} c\epsilon_0 |\boldsymbol{\mathcal{E}}(x,y)|^2}{\iint_\infty Re\{\boldsymbol{\mathcal{E}} \times \boldsymbol{\mathcal{H}}^*\}\cdot\hat{\mathbf{z}}dA} u_E dA}{\int u_E dA}\right]P \tag{4.19}$$

Or equivalently,

$$\Delta\tilde{\beta} = \frac{\omega}{c}\left(\mathrm{n}_2 + i\frac{4\pi}{\lambda_0}\beta_T\right)\left[\frac{\iint_{\mathcal{A}} \frac{(n_{\mathcal{A}} c\epsilon_0)^2 |\boldsymbol{\mathcal{E}}(x,y)|^4}{\iint_\infty Re\{\boldsymbol{\mathcal{E}} \times \boldsymbol{\mathcal{H}}^*\}\cdot\hat{\mathbf{z}}dA} dA}{\iint_\infty Re\{\boldsymbol{\mathcal{E}} \times \boldsymbol{\mathcal{H}}^*\}\cdot\hat{\mathbf{z}}dA}\right]P \tag{4.20}$$

Pulling all spatially invariant terms out of the integral, and dividing by *P* we may write:

$$\frac{\Delta\tilde{\beta}}{P} = \tilde{\gamma} = \frac{\omega}{c}\left(\mathrm{n}_2 + i\frac{4\pi}{\lambda_0}\beta_T\right)\left[(n_{\mathcal{A}} c\epsilon_0)^2 \frac{\int |\boldsymbol{\mathcal{E}}(x,y)|^4 dA}{\left(\iint_\infty Re\{\boldsymbol{\mathcal{E}} \times \boldsymbol{\mathcal{H}}^*\}\cdot\hat{\mathbf{z}}dA\right)^2}\right] \tag{4.21}$$

Given that the nonlinear parameter is written in terms of the effective mode area via:

$$\frac{\Delta\tilde{\beta}}{P} = \tilde{\gamma} = \frac{\omega}{c}\left(\mathrm{n}_2 + i\frac{4\pi}{\lambda_0}\beta_T\right)\frac{1}{A_{eff}^{(NL)}} \tag{4.22}$$

The nonlinear effective mode area can be found to be:

$$A_{eff}^{(NL)} = \frac{1}{n_{\mathcal{A}}^2 c^2 \epsilon_0^2} \frac{\left(\iint_{\infty} Re\{\boldsymbol{\mathcal{E}} \times \boldsymbol{\mathcal{H}}^*\} \cdot \hat{\mathbf{z}} dA \right)^2}{\int |\boldsymbol{\mathcal{E}}(x,y)|^4 dA} \tag{4.23}$$

Where the numerator can alternatively be expressed as:

$$\left(\iint_{\infty} Re\{\boldsymbol{\mathcal{E}} \times \boldsymbol{\mathcal{H}}^*\} \cdot \hat{\mathbf{z}} dA \right)^2 = \left(\frac{c}{n_g} \iint_{\infty} \frac{\partial}{\partial \omega} (\omega \epsilon) |\boldsymbol{\mathcal{E}}|^2 dA \right)^2 \tag{4.24}$$

Which yields:

$$A_{eff}^{(NL)} = \frac{1}{n_{\mathcal{A}}^2 n_g^2 \epsilon_0^2} \frac{\left(\iint_{\infty} \frac{\partial}{\partial \omega} (\omega \epsilon) |\boldsymbol{\mathcal{E}}|^2 dA \right)^2}{\int |\boldsymbol{\mathcal{E}}(x,y)|^4 dA} \tag{4.25}$$

Which in the approximation of low material dispersion, can be simplified to:

$$A_{eff}^{(NL)} = \frac{1}{n_{\mathcal{A}}^2 n_g^2} \frac{\left(\iint_{\infty} n^2 |\boldsymbol{\mathcal{E}}|^2 dA \right)^2}{\iint_{\mathcal{A}} |\boldsymbol{\mathcal{E}}|^4 dA} \tag{4.26}$$

This expression agrees with the nonlinear effective mode area derived for photonic crystal fibers [48] and is much simpler than Eq. (4.9). Upon close inspection of Eqs. (4.9) and (4.26), the above expression if found to be equivalent to:

$$A_{eff}^{(NL)} = \frac{1}{\Gamma_{\mathcal{A}}^2}\frac{\left(\iint_{\mathcal{A}} |\boldsymbol{\mathcal{E}}|^2 dA\right)^2}{\iint_{\mathcal{A}} |\boldsymbol{\mathcal{E}}|^4 dA} = \frac{1}{(U_{\mathcal{A}}\mathcal{A})^2}\frac{\left(\iint_{\mathcal{A}} |\boldsymbol{\mathcal{E}}|^2 dA\right)^2}{\iint_{\mathcal{A}} |\boldsymbol{\mathcal{E}}|^4 dA} \tag{4.27}$$

Which is the formula presented in, Eq. (2.3). This form of the nonlinear effective mode area shows that the nonlinearity can be explicitly linked to the confinement factor utilized in *linear* optics. The right most term is effectively a field correction term which ensures integration is performed over the $|\boldsymbol{\mathcal{E}}|^4$ profile rather than the $|\boldsymbol{\mathcal{E}}|^2$ profile. Given that $\Gamma_{\mathcal{A}}^2 = (U_{\mathcal{A}}\mathcal{A})^2$ the nonlinear effective mode area can also be directly linked to the optical concentration.

With Eq. (4.27) in hand we can rewrite Eq. (4.22) directly in terms of optical concentration and active area:

$$\frac{\Delta\tilde{\beta}}{P} = \tilde{\gamma} = \frac{\omega}{c}\left(\mathrm{n}_2 + i\frac{4\pi}{\lambda_0}\beta_T\right)\frac{(U_{\mathcal{A}}\mathcal{A})^2 \iint_{\mathcal{A}} |\boldsymbol{\mathcal{E}}|^4 dA}{\left(\iint_{\mathcal{A}} |\boldsymbol{\mathcal{E}}|^2 dA\right)^2} \tag{4.28}$$

Here, in this chapter the nonlinear effective mode area has been derived in terms of optical concentration, a new figure of merit. This definition is particularly important since, the performance of any nonlinear photonic devices rely on the mode area. The optical concentration as defined in the previous chapter depend on the electric field energy density u_E and confinement factor $\Gamma_{\mathcal{A}}$, the nonlinear effective mode area also depends on u_E and $\Gamma_{\mathcal{A}}$.

CHAPTER 5

NUMERICAL EVALUATION AND INTERPRETATION OF EXTREME OPTICAL CONCENTRATION

Optical concentration, a new figure of merit for nanophotonics has been derived rigorously in the previous chapters. In this chapter, this new metric has been evaluated and analyzed for the proposed diabolo and V-groove structures in this work for different active areas of high index region (silicon). These results are then benchmarked against a Si-Ag nano-rib plasmonic waveguide structure, which exhibits an ultra-small mode area and strong confinement factor within silicon. Our proposed diabolo and V-groove structures are benchmarked against this plasmonic structure to evaluate the performance comparisons. The measured optical concentration for diabolo, V-groove and Si-Ag plasmonic nano-rib structures have been presented and compared in this chapter and finally a conclusion has been drawn.

5.1 Method

To assess the characteristics of different waveguides we compute their modal properties using a commercially available eigenmode solver (Lumerical MODE). Mode properties are then determined by numerical evaluation of the appropriate equation noted in previous sections. All calculations are performed at λ_0 = 1550 nm. All models assume the refractive indices of Si, SiO_2, and air to be 3.5, 1.444, and 1.0 respectively, while the complex relative permittivity of Ag in the plasmonic benchmark model is taken from Palik [56]. Unless otherwise noted, all calculations involving groove tips or corners are modelled with a realistic non-zero radius of curvature r = 3 nm and an

ultra-fine local mesh size of 0.2 nm to ensure a fully converged mode solution which yields accurate and stable results. The groove angles are set to 54.7 degrees to mimic the potential shape of a wet etched {100} silicon microstructure [43,44]. This approach eliminates the non-physical singularity that would occur for *r* = 0 nm corners [5,57], which would result, for example, in a non-convergent calculation of A_n with reducing mesh size. This same principle is applied to the slot waveguide mode area calculation in Fig. 2.2(ii), wherein the maximum energy density is taken from the middle of the structure and not the corner singularities as done in Ref. [5].

The modal properties of the proposed diabolo and V-groove structures (classic mode area, nonlinear effective mode area, group and effective indices and confinement factor in the active region) for different width of high index bridge "*h*" and groove tip radius of curvature "*r*" have been computed and presented in chapter 2 (Fig. 2.3 and Fig. 2.4).

5.2 Singularities at *r = 0 nm*

In the simulations of this work, the groove tips of both the V-groove structure and the diabolo structure have been modelled with a radius of curvature of r = 3 nm. Because of this modelling, the groove tips become circular instead of pointed. This is done intentionally to eliminate the singularity. In our simulation, ultra-fine mesh size has been used (0.2 nm). With this mesh size when simulation is performed at the pointed tip groove structure (both V-groove and diabolo structure), singularity occurs. Due to this singularity, electric field becomes infinite resulting in unreal very small effective mode area. To solve this problem, the groove tips have been rounded with radius of curvature, r = 3 nm, which eliminates this singularity. Fig. 5.1 shows the

schematic diagram of the V-groove and diabolo structure with radius of curvature, r = 3 nm and r = 0 nm.

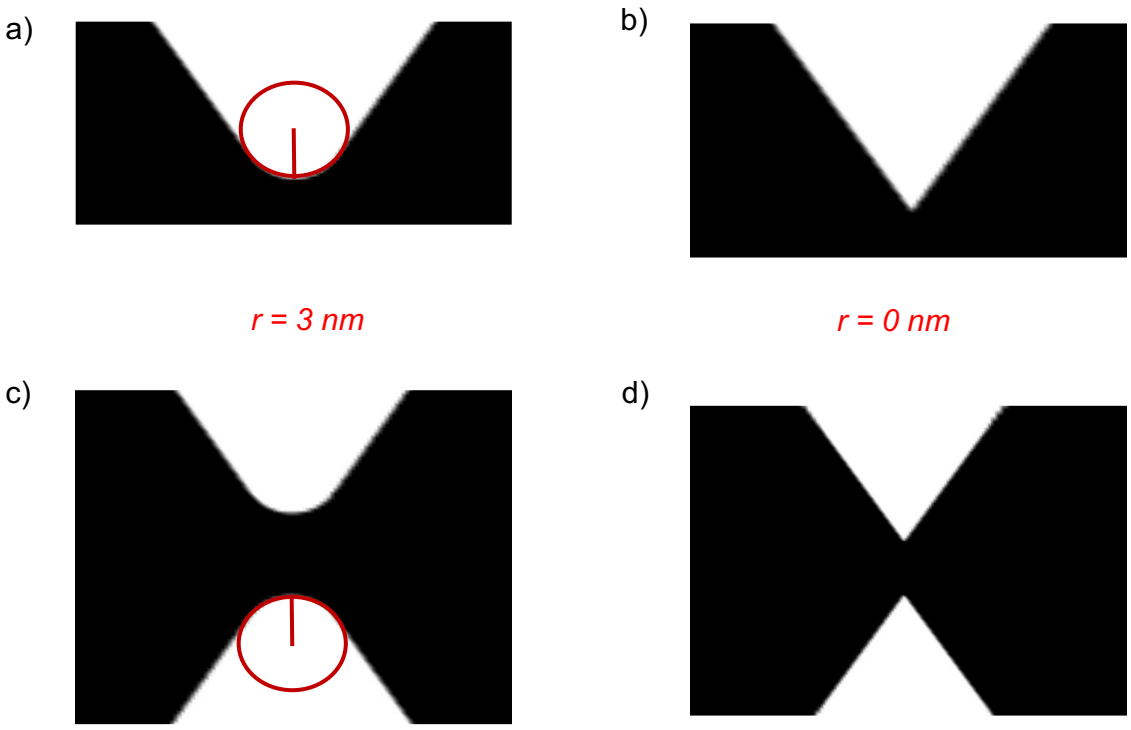

Fig. 5.1: Schematic diagram of a) V-groove (r = 3nm), b) V-groove (r = 0nm), c) Diabolo (r = 3nm) and d) Diabolo (r = 0nm) structure

5.3 Results

Fig. 5.2 depicts the computed optical concentration, in silicon, of air-clad diabolo and V-groove waveguides with small silicon bridge heights, *h* = 2 nm and 20 nm, benchmarked against the silicon strip waveguide of Fig. 2.2(i) and a hybrid dielectric-nanoplasmonic Si-Ag structure from the recent literature [24] (section 5.4). The optical concentration $U_{\mathcal{A}}$ is computed via numerical evaluation of Eq. (3.7), wherein the active area $\mathcal{A}$ is swept over a large range of possible shapes/sizes within

the silicon cross-section. For large $\mathcal{A}$, comparable to or larger in scale than the diffraction limit $(\lambda_n/2)^2$, $U_{\mathcal{A}}$ cannot be enhanced through the transverse plasmonic, dielectric, or metamaterial design owing to energy conservation and mode normalization. This is observed mathematically in the $\gamma_{\mathcal{A}}/\mathcal{A}$ term from Eq. (3.7). Thus, in the regime of large $\mathcal{A}$, the only tools available to significantly enhance optical concentration are to reduce the group velocity or recirculate light [16,41,53].

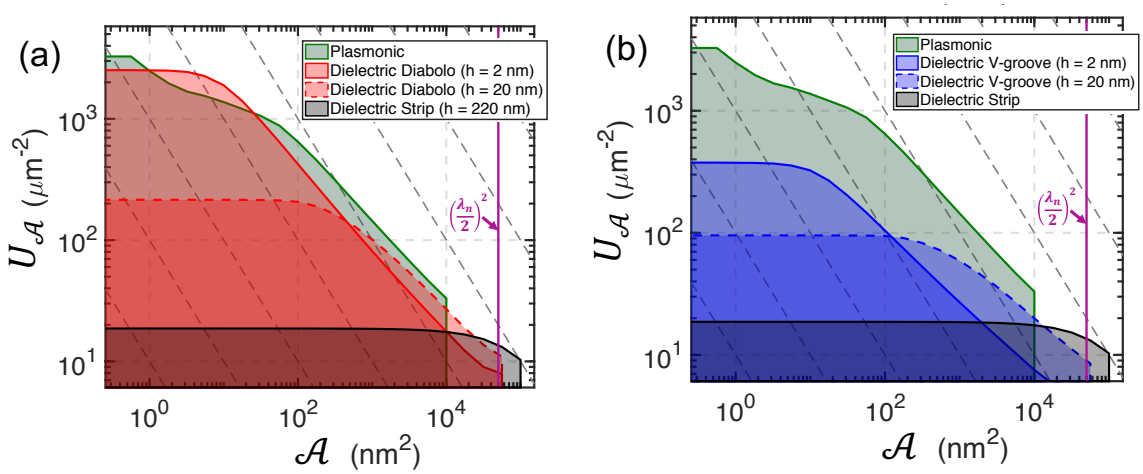

Fig. 5.2. All-dielectric sub-diffraction enhancement in optical concentration. The optical concentration (in silicon) is computed numerically via Eq. (3.7) vs. active area dimensions, for reference dielectric strip (500 x 220 nm) and plasmonic waveguides; and compared to air cladded silicon: (a) diabolo and (b) V-groove waveguides. Dashed diagonal lines indicate constant $U_{\mathcal{A}}\mathcal{A} = \Gamma_{\mathcal{A}}$ contours.

For small $\mathcal{A} < (\lambda_n/2)^2$ however, transverse structuring of the dielectric function, and enforcement of vectorial boundary conditions, allows the electric field energy to be significantly redistributed and locally enhanced. This enables the V-groove and diabolo waveguides to achieve extreme optical concentrations

$U_{\mathcal{A}} \sim 10^2\ \mu m^{-2}$ to $10^3\ \mu m^{-2}$. Remarkably, we observe the optical concentration of the air-clad diabolo waveguide closely rivals, or in some cases even exceeds the plasmonic benchmark. Thus, while both the plasmonic and diabolo waveguides achieve a 'classic' A_n on the order of $\sim\lambda_0^2/10{,}000$, when considering $\boldsymbol{r}_{max}$ from Eq. (3.9) is in silicon, the plasmonic structure exhibits a theoretical propagation loss of ~10^4 dB cm^{-1} while the all-dielectric diabolo is theoretically lossless.

The optical concentration profiles in Fig. 5.2 show clear plateaus where further reducing $\mathcal{A}$ provides diminishing and ultimately negligible improvement in $U_{\mathcal{A}}$. This is associated with the active dimensions becoming comparable to and ultimately smaller than the extent of the localized u_E enhancement. In a strip waveguide, this plateau occurs in the vicinity of the diffraction limit, e.g. near $\mathcal{A} \approx 10^4$ nm^2. Such an active area could be realized with a ~100 nm x 100 nm active region, or with some slight penalty a ~45 nm x 220 nm active region. Such dimensions are comparable to the active regions of state-of-the-art *pn* diode electro-optic modulators [54]. While the active regions of such devices can be made larger to increase $\Gamma_{\mathcal{A}}$, i.e. using wider depletion regions or wrapped junctions [54,55], this only optimizes the device length *l*, i.e. Eq. (3.5), and in fact penalizes the optical concentration $U_{\mathcal{A}}$. Per Eq. (3.8), any reduction in $U_{\mathcal{A}}$ must be met with an increase in active volume $\mathcal{V}$ to achieve the desired optical response. Similarly, any device which can achieve a larger $U_{\mathcal{A}}$ enables the optical response to be achieved with a lower active volume $\mathcal{V}$. An important implication of this, is that the diabolo or V-groove waveguide, for example, could principally enable reduction in the active volume of a state-of-the-art silicon diode phase shifter by a factor of ~10-100. Crucially, this does not require a plasmonic

structure to be utilized and can therefore potentially be realized with the low optical losses typically associated with all-dielectric media. Given that the grooves are in principle amenable to fabrication via anisotropic wet etching of silicon [43,44], we expect that very smooth surfaces can ultimately be realized – much smoother than traditional reactive ion-etched sidewalls. Thus, it's plausible to expect optical losses might be on par with the ~dB cm^{-1} scale losses of standard silicon nanowires.

The silicon phase shifter, however, is only one niche example of the implications of achieving an extreme optical concentration [34]. The exact same efficiency and active volume scaling principles apply to the design of waveguide integrated light emitters and absorbers. It should also be noted that in many practical cases of interest a ~10x enhancement in $U_{\mathcal{A}}$, for example, may require working with a ~100x reduction in $\mathcal{A}$. Perhaps counterintuitively, this configuration enables a reduction in total active volume $\mathcal{V}$ of ~10x but requires simultaneously *lengthening* the device by a factor of ~10x. This highlights the significance of the transverse device dimensions, which in fact control 2 out of 3 spatial degrees of freedom. In device applications where $\mathcal{A}$ is already very small for fundamental reasons (i.e. atom-light interfaces, integrated 2D atomic materials, quantum wells, etc.) then ~10-100x enhancement in $U_{\mathcal{A}}$ is feasible under constant $\mathcal{A}$. In such cases, the efficiency *and* length of the device can be improved by the ~10-100x factor relative to a diffraction limited waveguide. As a powerful example, one could already imagine a diabolo or V-groove bridge, with height *h*, being formed entirely out of a single sub-nanometer thickness high index 2D atomic monolayer. The enforcement of vectorial boundary conditions would constrain the mode solution to yield unprecedented low-loss optical

concentration in the active nanomaterial. These results and observations clearly indicate that continued investigations into the regime of deeply sub-wavelength dielectric nanophotonics are warranted and will likely yield new generations of ultra-efficient linear and nonlinear devices.

5.4 Hybrid dielectric-nanoplasmonic Si-Ag structure

The proposed diabolo and V-groove structures have been benchmarked against the dielectric-nanoplasmonic Si-Ag structure [24]. This hybrid nano-rib structure is shown schematically in Fig. 5.3. This hybrid nano-rib structure is made of a metallic nanowire located above silicon nano-rib waveguide. A thin silicon dioxide layer is deposited over the silicon slab. As a result, a hybrid, nonuniform, low-index gap is formed between the metal nanowire and lower silicon substrate. For the metal nanowire, silver (Ag) is used in this design. This hybrid, nonuniform, low-index gap induces the coupling between the nanowire plasmon and the silicon nano-rib photonic modes [24].

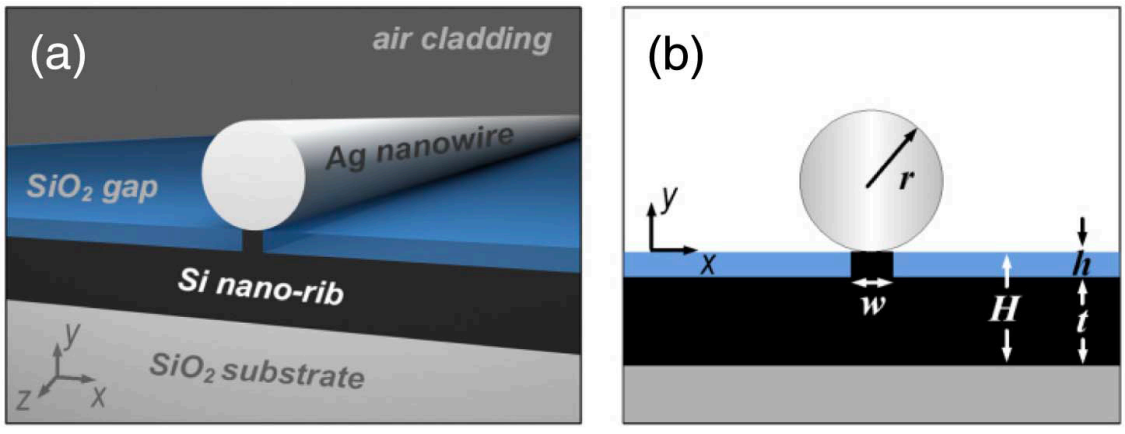

Fig. 5.3: Hybrid nanowire-loaded silicon nano-rib waveguide, a) Schematic of the 3D geometry, b) Cross-section of the configuration on *x-y* plane [24]

The simulation of this hybrid-nanoplasmonic structure is done in Lumerical Mode Solution. In the simulations, the refractive indices of silicon dioxide, silicon, air and silver are considered as: 1.444, 3.476, 1 and 0.47+9.32i (Palik model) [56]. The simulation is done for 1550nm wavelength excitation. This wavelength is chosen for our simulation, because in the next step of our work we are going to fabricate and test these devices, and for testing purposes 1550 nm sources will be used. So, to compare the test results to the simulation results, all the simulations have been performed at 1550 nm wavelengths.

In the design of this hybrid-nanoplasmonic Si-Ag structure, the radius of the Ag nanowire, r = 75 nm; nano-rib width, w = 10 nm; nano-rib height, h = 5 nm and Si waveguide thickness, t = 60 nm [24]. The optical concentration for this hybrid dielectric-nanoplasmonic Si-Ag structure has also been evaluated and benchmarked against the optical concentration of proposed diabolo and V-groove structure as shown in Fig. 5.2.

CHAPTER 6

CONCLUSION AND FUTURE WORKS

6.1 Conclusion

In summary, we have introduced a simple approach for designing all-dielectric waveguides capable of achieving significantly enhanced linear and nonlinear interactions. Moreover, we have laid out the theory of optical concentration in the context of waveguides and shown its convenient and unifying characteristics in describing the performance of linear and nonlinear devices with arbitrary active dimensions.

The principle physics investigated here and detailed in Chapter 2, rely on vectorial boundary conditions to Maxwell's equations. Indeed, the vector nature of light offers a powerful tool for tailoring light-matter interactions at the nanoscale, giving rise to birefringence, surface plasmon and slot waveguide field and energy density enhancements, metamaterial effects, deep sub-diffraction photonic crystal mode volume reduction, and now all-dielectric waveguide field and energy density enhancements accessible by high index media. We envision a wide array of scientific and technological applications that may benefit from the now expanded nanophotonic 'toolkit', including for example ultra-efficient integrated photonic active devices in both planar (e.g. nanowire) and arrayed (e.g. meta/nano-pillar) formats; high efficiency sources of classical and quantum light; broadband, slow-light, or resonant nonlinear optical devices; and more.

6.2 Future works

In this work, the theory of novel waveguide structures has been presented. The next logical step is to fabricate these novel V-groove and diabolo structures, characterize their properties, and implement functional nanophotonic devices. In addition to this, a variety of additional questions also arise which need to be addressed both theoretically and experimentally. For example, how does one efficiently couple to the ultra-small mode area V-groove waveguide detailed in Chapter 2? Recent work by our group has demonstrated that evanescent coupling provides an attractive solution for coupling between dissimilar optical modes [59]. More recent work indicates that compact adiabatic directional couplers which efficiently couple to ultra-small mode area waveguides with broadband characteristics and good fabrication tolerances are possible [59]. Below is a summary of key research topics/questions and experimental demonstrations which could be directly pursued subsequent to this work:

- Develop scalable nanomanufacturing approaches for realizing V-groove and diabolo waveguides
- Experimental characterization of waveguide properties
- Demonstration of high-performance optical couplers for interfacing to V-groove and diabolo waveguides
- Construction of linear and nonlinear devices based on V-groove and diabolo waveguide building blocks

A key early question that needs to be addressed are the real-world optical propagation losses of these novel waveguides. While theoretically lossless, similar technologies i.e. slot waveguides have been shown to exhibit enhanced optical losses

owing to increased light-matter interaction with the waveguide surface roughness. As discussed in Chapter 2, we anticipate that wet-etch fabrication techniques will enable very smooth V-groove and diabolo surfaces to be realized. Optimization of this roughness will be an important topic for the practical realization of low-loss optical components with ultra-small mode dimensions and extreme optical concentrations. The fabrication process flow of the diabolo and V-groove waveguide structure is illustrated as follows:

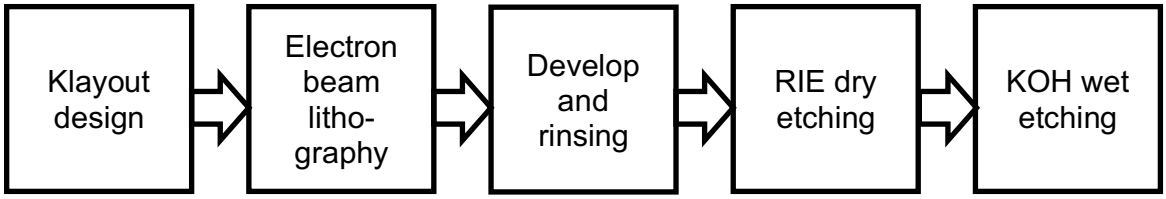

Fig. 6.1: Fabrication process flow of diabolo and V-groove waveguide

The KOH wet etching of silicon is crystal orientation dependent. The etch rate for <100> crystal orientation is higher compared to <111> or <110> crystal orientation. As a result, when KOH etching is done, a groove is formed with an angle of 54.7-degree with the surface. This groove is formed because of the silicon crystal properties towards KOH wet etching. This is the reason, 54.7-degree angle has been used in the simulation to mimic the actual device structure. The etch depth depends on etch time and temperature. Silicon nitride is also used for hard mask.

Fig. 6.2 shows the cross-sectional diagram of an example V-groove structure realized from anisotropic wet etching of <100> silicon in KOH. So far, we have established a stable fabrication recipe, but this recipe needs some modification. We

expect that variants of this process could be used to realize diabolo structures in addition to the V-groove structures. Finally, these structures will ultimately need to be placed in the silicon waveguide alongside more complex structures (e.g. interferometers, gratings, and couplers) to realize whole devices and photonic circuits.

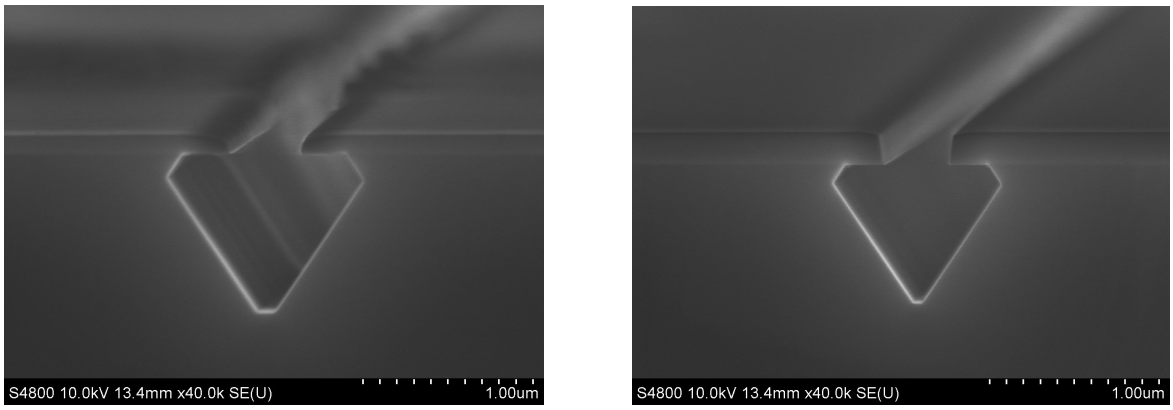

Fig. 6.2: SEM images of V-groove structures

REFERENCES

[1] G.T. Reed, G. Mashanovich, F.Y. Gardes, and D.J. Thomson, "*Silicon optical modulators*," *Nat. Photonics* **4**, 8 (2010).

[2] M. Eichenfield, J. Chan, R.M. Camacho, K.J. Vahala, and O. Painter, "*Optomechanical crystals.*," *Nature* **462**, 7269 (2009).

[3] M. SoljaČiĆ and J.D. Joannopoulos, "*Enhancement of nonlinear effects using photonic crystals*," *Nat. Mater.* **3**, 4 (2004).

[4] J. Leuthold, C. Koos, W. Freude, R. Osgood, J. Leuthold, C. Koos, and W. Freude, "*Nonlinear silicon photonics*," *Nat. Photonics* **4**, 8 (2010).

[5] H. Choi, M. Heuck, and D. Englund, "*Self-Similar Nanocavity Design with Ultrasmall Mode Volume for Single-Photon Nonlinearities*," *Phys. Rev. Lett.* **118**, 22 (2017).

[6] D.E. Chang, V. Vuletić, and M.D. Lukin, "*Quantum nonlinear optics - Photon by photon*," *Nat. Photonics* **8**, 9 (2014).

[7] A.H.J. Yang, S.D. Moore, B.S. Schmidt, M. Klug, M. Lipson, and D. Erickson, "*Optical manipulation of nanoparticles and biomolecules in sub-wavelength slot waveguides*," *Nature* **457**, 7225 (2009).

[8] T.H. Talukdar, G.D. Allen, I. Kravchenko, and J.D. Ryckman, "*Single-mode porous silicon waveguide interferometers with unity confinement factors for ultra-sensitive surface adlayer sensing*," *Opt. Express* **27**, 16 (2019).

[9] J.T. Robinson, L. Chen, and M. Lipson, "*On-chip gas detection in silicon optical microcavities*," *Opt. Express* **16**, 6 (2008).

[10] R.-M. Ma and R.F. Oulton, "*Applications of nanolasers*," *Nat. Nanotechnol.* **14**.

[11] D.J. Bergman and M.I. Stockman, "*Surface Plasmon Amplification by Stimulated Emission of Radiation: Quantum Generation of Coherent Surface Plasmons in Nanosystems*," *Phys. Rev. Lett.* **90**, 2 (2003).

[12] C. Sauvan, J.P. Hugonin, I.S. Maksymov, and P. Lalanne, "*Theory of the Spontaneous Optical Emission of Nanosize Photonic and Plasmon Resonators*," (2013).

[13] P. Kolchin, N. Pholchai, M.H. Mikkelsen, J. Oh, S. Ota, M.S. Islam, X. Yin, and X. Zhang, "*High Purcell Factor Due To Coupling of a Single Emitter to a Dielectric Slot Waveguide*," *Nano Lett.* **15**, 1 (2015).

[14] J.P. Zhang, D.Y. Chu, S.L. Wu, S.T. Ho, W.G. Bi, C.W. Tu, and R.C. Tiberio, "*Photonic-Wire Laser*," *Phys. Rev. Lett.* **75**, 14 (1995).

[15] A.S. Liu, R. Jones, L. Liao, D. Samara-Rubio, D. Rubin, O. Cohen, R. Nicolaescu, and M. Paniccia, "*A high-speed silicon optical modulator based on a metal-oxide-semiconductor capacitor*," *Nature* **427**, 6975 (2004).

[16] Q.F. Xu, B. Schmidt, S. Pradhan, and M. Lipson, "*Micrometre-scale silicon electro-optic modulator*," *Nature* **435**, 7040 (2005).

[17] M. Liu, X.B. Yin, E. Ulin-Avila, B.S. Geng, T. Zentgraf, L. Ju, F. Wang, and X. Zhang, "*A graphene-based broadband optical modulator*," *Nature* **474**, 7349 (2011).

[18] W. Heni, Y. Fedoryshyn, B. Baeuerle, A. Josten, C.B. Hoessbacher, A. Messner, C. Haffner, T. Watanabe, Y. Salamin, U. Koch, D.L. Elder, L.R. Dalton, and J. Leuthold, "*Plasmonic IQ modulators with attojoule per bit electrical energy consumption*," *Nat. Commun.* **10**, 1 (2019).

[19] S. Assefa, F. Xia, S.W. Bedell, Y. Zhang, T. Topuria, P.M. Rice, and Y.A. Vlasov, "*CMOS-integrated high-speed MSM germanium waveguide photodetector*," *Opt. Express* **18**, 5 (2010).

[20] A. Goban, C.L. Hung, S.P. Yu, J.D. Hood, J.A. Muniz, J.H. Lee, M.J. Martin, A.C. McClung, K.S. Choi, D.E. Chang, O. Painter, and H.J. Kimble, "*Atom-light interactions in photonic crystals*," *Nat. Commun.* **5**, May (2014).

[21] D.F.P. Pile, T. Ogawa, D.K. Gramotnev, Y. Matsuzaki, K.C. Vernon, K. Yamaguchi, T. Okamoto, M. Haraguchi, and M. Fukui, "*Two-dimensionally localized modes of a nanoscale gap plasmon waveguide*," *Appl. Phys. Lett.* **87**, 26 (2005).

[22] R.F. Oulton, V.J. Sorger, D.A. Genov, D.F.P. Pile, and X. Zhang, "*A hybrid plasmonic waveguide for subwavelength confinement and long-range propagation*," *Nat. Photonics* **2**, 8 (2008).

[23] D.K. Gramotnev and S.I. Bozhevolnyi, "*Plasmonics beyond the diffraction limit*," *Nat. Photonics* **4**, 2 (2010).

[24] Y.U.B. Ian and Q.I.R. En, "*Deep-subwavelength light transmission in hybrid nanowire-loaded silicon nano-rib waveguides*," *Photonics Res.* **6**, 1 (2018).

[25] S. Jahani and Z. Jacob, "*Transparent subdiffraction optics : nanoscale light confinement without metal*," *Optica* **1**, 2 (2014).

[26] V.R. Almeida, Q. Xu, C.A. Barrios, and M. Lipson, "*Guiding and confining light in void nanostructure*," *Opt. Lett.* **29**, 11 (2004).

[27] S.A. Maier and H.A. Atwater, "*Plasmonics: Localization and guiding of electromagnetic energy in metal/dielectric structures*," *J. Appl. Phys.* **98**, 1.

[28] G.S. Wiederhecker, C.M.B. Cordeiro, F. Couny, F. Benabid, S.A. Maier, J.C. Knight, C.H.B. Cruz, and H.L. Fragnito, "*Field enhancement within an optical fibre with a subwavelength air core*," *Nat. Photonics* **1**, 2 (2007).

[29] A.W. Fang, H. Park, O. Cohen, R. Jones, M.J. Paniccia, and J.E. Bowers, "*Electrically pumped hybrid AlGaInAs-silicon evanescent laser*," *Opt. Express* **14**, 20 (2006).

[30] S. Strauf, N.G. Stoltz, M.T. Rakher, L.A. Coldren, P.M. Petroff, and D. Bouwmeester, "*High-frequency single-photon source with polarization control*," *Nat. Photonics* **1**, 12 (2007).

[31] J.D. Ryckman, K.A. Hallman, R.E. Marvel, R.F. Haglund Jr., and S.M. Weiss, "*Ultra-compact silicon photonic devices reconfigured by an optically induced semiconductor-to-metal transition*," *Opt. Express* **21**, 9 (2013).

[32] S. Hu and S.M. Weiss, "*Design of Photonic Crystal Cavities for Extreme Light Concentration*," *ACS Photonics* **3**, 9 (2016).

[33] S. Hu, M. Khater, R. Salas-montiel, E. Kratschmer, S. Engelmann, W.M.J. Green, and S.M. Weiss, "*Experimental realization of deep-subwavelength confinement in dielectric optical resonators*," *Sci. Adv.* **4**, eaat2355 (2018).

[34] D.A.B. Miller, "*Attojoule Optoelectronics for Low-Energy Information Processing and Communications*," *J. Light. Technol.* **35**, 3 (2017).

[35] E.M. Purcell, H.C. Torrey, and R. V Pound, "*Resonance Absorption by Nuclear Magnetic Moments in a Solid*," *Phys. Rev.* **69**, 1–2 (1946).

[36] E.A. Muljarov and W. Langbein, "*Exact mode volume and Purcell factor of open optical systems*," *Phys. Rev. B* **94**, (2016).

[37] J.-M. Liu, "*Photonic Devices*," (n.d.).

[38] A. Berk, "*Variational principles for electromagnetic resonators and waveguides*," *IRE Trans. Antennas Propag.* **4**, 2 (1956).

[39] M.A. Biot, "*General Theorems on the Equivalence of Group Velocity and Energy Transport*," *Phys. Rev.* **105**, 4 (1957).

[40] J.T. Robinson, K. Preston, O. Painter, and M. Lipson, "*First-principle derivation of gain in high-index- contrast waveguides*," *Opt. Express* **16**, 21 (2008).

[41] Y.-C. Chang, S.P. Roberts, B. Stern, I. Datta, and M. Lipson, Resonance–Free Light Recycling in Waveguides, in: Conf. Lasers Electro-Optics, Optical Society of America, San Jose, California (2017), p. SF1J.5.

[42] Y.-C. Chang, S.A. Miller, C.T. Phare, M.C. Shin, M. Zadka, S.P. Roberts, B. Stern, X. Ji, A. Mohanty, O.A.J. Gordillo, and M. Lipson, Scalable low-power silicon photonic platform for all-solid-state beam steering, in: Proc. SPIE, (2019).

[43] Z. Wang, B. Tian, M. Pantouvaki, W. Guo, P. Absil, J. Van Campenhout, C. Merckling, and D. Van Thourhout, "*Room-temperature InP distributed feedback laser array directly grown on silicon*," *Nat. Photonics* **9**, 12 (2015).

[44] S. Migita, Y. Morita, M. Masahara, and H. Ota, "*Fabrication and Demonstration of 3-nm-Channel-Length Junctionless Field-Effect Transistors on Silicon-on-Insulator Substrates Using Anisotropic Wet Etching and Lateral Diffusion of Dopants*," *Jpn. J. Appl. Phys.* **52**, 4S (2013).

[45] M.A. Foster, K.D. Moll, and A.L. Gaeta, "*Optimal waveguide dimensions for nonlinear interactions*," *Opt. Express* **12**, 13 (2004).

[46] C. Monat, B. Corcoran, M. Ebnali-Heidari, C. Grillet, B.J. Eggleton, T.P. White, L. O'Faolain, and T.F. Krauss, "*Slow light enhancement of nonlinear effects in silicon engineered photonic crystal waveguides*," *Opt. Express* **17**, 4 (2009).

[47] K. Guo, S.M.M. Friis, J.B. Christensen, E.N. Christensen, X. Shi, Y. Ding, H. Ou, and K. Rottwitt, "*Full-vectorial propagation model and modified effective mode area of four-wave mixing in straight waveguides*," *Opt. Lett.* **42**, 18 (2017).

[48] J. Lægsgaard, N.A. Mortensen, and A. Bjarklev, "*Mode areas and field-energy distribution in honeycomb photonic bandgap fibers*," *J. Opt. Soc. Am. B* **20**, 10 (2003).

[49] M. de Cea, A.H. Atabaki, and R.J. Ram, "*Power handling of silicon microring modulators*," *Opt. Express* **27**, 17 (2019).

[50] V.R. Almeida and M. Lipson, "*Optical bistability on a silicon chip*," *Opt. Lett.* **29**, 20 (2004).

[51] A. Sipahigil, R.E. Evans, D.D. Sukachev, M.J. Burek, J. Borregaard, M.K. Bhaskar, C.T. Nguyen, J.L. Pacheco, H.A. Atikian, C. Meuwly, R.M. Camacho, F. Jelezko, E. Bielejec, H. Park, M. Lončar, and M.D. Lukin, "*An integrated diamond nanophotonics platform for quantum-optical networks*," *Science* **354**, 6314 (2016).

[52] M.K. Bhaskar, D.D. Sukachev, A. Sipahigil, R.E. Evans, M.J. Burek, C.T. Nguyen, L.J. Rogers, P. Siyushev, M.H. Metsch, H. Park, F. Jelezko, M. Lončar, and M.D. Lukin, "*Quantum Nonlinear Optics with a Germanium-Vacancy Color Center in a Nanoscale Diamond Waveguide*," *Phys. Rev. Lett.* **118**, 22 (2017).

[53] F. Riboli, P. Bettotti, and L. Pavesi, "*Band gap characterization and slow light effects in one dimensional photonic crystals based on silicon slot-waveguides*," *Opt. Express* **15**, 19 (2007).

[54] E. Timurdogan, C.M. Sorace-Agaskar, J. Sun, E. Shah Hosseini, A. Biberman, and M.R. Watts, "*An ultralow power athermal silicon modulator*," *Nat. Commun.* **5**, (2014).

[55] Z. Yong, W.D. Sacher, Y. Huang, J.C. Mikkelsen, Y. Yang, X. Luo, P. Dumais, D. Goodwill, H. Bahrami, P.G.-Q. Lo, E. Bernier, and J.K.S. Poon, "*U-shaped PN junctions for efficient silicon Mach-Zehnder and microring modulators in the O-band*," *Opt. Express* **25**, 7 (2017).

[56] E.D. Palik, “Handbook of optical constants of solids”, Academic press, (1998).

[57] H. Shi, Y.Y. Lu, and Q. Du, "*Calculating corner singularities by boundary integral equations*," *J. Opt. Soc. Am. A* **34**, 6 (2017).

[58] X. Guan, X. Wang and L.H. Frandsen, “*Optical temperature sensor with enhanced sensitivity by employing hybrid waveguides in a silicon Mach-Zehnder interferometer*”, *Opt. Express* **24,** 15 (2016).

[59] F.B. Tarik, and J.D. Ryckman, *“Efficient optical coupling to ultra-low mode area silicon V-groove waveguides”*

[60] D. Andrea, "CMOS Photonics Today & Tomorrow Enabling Technology," in Proc. OFC, 2009, San Diego, 2009.

[61] F.Y. Gardes, G.T. Reed, N.G. Emerson, and C.E. Png, “A sub-micron depletion-type photonic modulator in silicon on insulator”, *Optics Express,* vol. 13, 2005.

[62] <http://www.fiber-optic-components.com/the-advantages-and-disadvantages-of-multimode-and-single-mode-fiber.html>

[63] J. Leuthold, C. Koos, W. Freude, R. Osgood, J. Leuthold, C. Koos, and W. Freude, "*Nonlinear silicon photonics*," *Nat. Photonics* **4**, 8 (2010).

[64] A.H.J. Yang, S.D. Moore, B.S. Schmidt, M. Klug, M. Lipson, and D. Erickson, *"Optical manipulation of nanoparticles and biomolecules in sub-wavelength slot waveguides", Nature 457, 71-75*